Geophysical Journal International

Geophys. J. Int. (2022) **230,** 480–506
Advance Access publication 2022 February 9
GJI Seismology

https://doi.org/10.1093/gji/ggac052

The $M_w = 6.6$ earthquake and tsunami of south Crete on 2020 May 2

Nikos Kalligeris [1], Vassilios Skanavis [2], Nikolaos S. Melis [1], Emile A. Okal [3], Aggeliki Dimitroulia,[4] Marinos Charalampakis [1], Patrick J. Lynett [5] and Costas E. Synolakis [2,5]

[1] *Institute of Geodynamics, National Observatory of Athens, Athens,* 11851, *Greece. E-mail: nkalligeris@noa.gr*
[2] *Academy of Athens, Athens,* 10680, *Greece*
[3] *Department of Earth and Planetary Sciences, Northwestern University, Evanston, IL,* 60208, *USA*
[4] *Department of Environmental Engineering, Technical University of Crete, Chania,* 73100, *Greece*
[5] *Department of Civil and Environmental Engineering, University of Southern California, Los Angeles, CA,* 90089, *USA*

Accepted 2022 February 7. Received 2022 January 28; in original form 2021 July 19

SUMMARY

On 2020 May 2, an $M_w = 6.6$ earthquake struck about 63 km south of Ierapetra in Crete, Greece. The earthquake generated a small tsunami which agitated local harbours. We studied this event in the context of earthquakes with seismic records in 1908, 1910, 1923, 1952, 2009 and 2013, all of similar magnitudes located south of Crete. Based on an energy-to-moment ratio, our analysis suggests that this event was neither slow nor fast, hence appropriate for using scaling laws to infer seafloor deformations. We also performed a field survey, three days after the event and present field observations from seven locations, including the island of Chrisi, where our highest measurement of 0.95 m was located. Runup along the coast of southern Crete ranged from 0.24 to 0.87 m. One tide gauge record is available for this event, and we did image analysis to obtain accurately timed water surface elevations from eyewitness videos and images. We undertook high-resolution hydrodynamic simulations using published moment tensor solutions to identify the source of the tsunami. Simulations were performed with two models, MOST (a nonlinear shallow water model) and COULWAVE (a Boussinesq-type model), to infer how different approximations of the parent equations of motion affect predictions for tsunamis of this size, which are fairly common in the Eastern Mediterranean and routinely trigger Tsunami Service Providers to issue warning messages. Based on the inter-model comparison, we conclude that the shallow-water equations are adequate in modelling this event at the distances considered, suggesting that such codes can be used to infer the tsunami source and to estimate tsunami impacts. Last, our field work revealed lack of knowledge of tsunami hazards, as most eyewitnesses remained near the waterfront, filming the associated unusual water motions instead of taking shelter on high ground.

Key words: Tsunamis; Europe; Image processing; Numerical modelling; Earthquake source observations.

1 INTRODUCTION

On 2020 May 2, at 12:51:09 UTC (15:51:09 local time), an underwater earthquake occurred approximately 63 km south of the coast of Crete, Greece. The moment tensor solution of the National Observatory of Athens (NOA) determined the earthquake magnitude to be $M_w = 6.6$, with a predominately thrust mechanism and the centroid located at 25.692°E, 34.437°N. The earthquake generation region is part of the central Hellenic arc. This is the most active geodynamic structure in the Mediterranean, and has produced the two largest earthquake-generated tsunamis in the historical record of the region, namely the 365 and 1303 A.D. tsunamis (Ambraseys & Synolakis 2010; England *et al.* 2015). Fault plane solutions produced by several seismological agencies (Fig. 1) also attributed the main shock to reverse type faulting, with a nearly E-W strike, indicative of the compressive tectonic regime in the area due to the subduction of the African plate below the Aegean, the ultimate episode of the closure of Tethys (e.g. Taymaz *et al.*, 1991). The earthquake-induced shaking was felt in many locales of Crete and nearby islands, but no casualties or damage to buildings were reported.

About 17 min after the earthquake, a series of tsunami waves of 0.33 m maximum wave height (peak to trough, Fig. 6b) arrived at the tide gauge of Ierapetra (25.7386°E, 35.0036°N, courtesy of

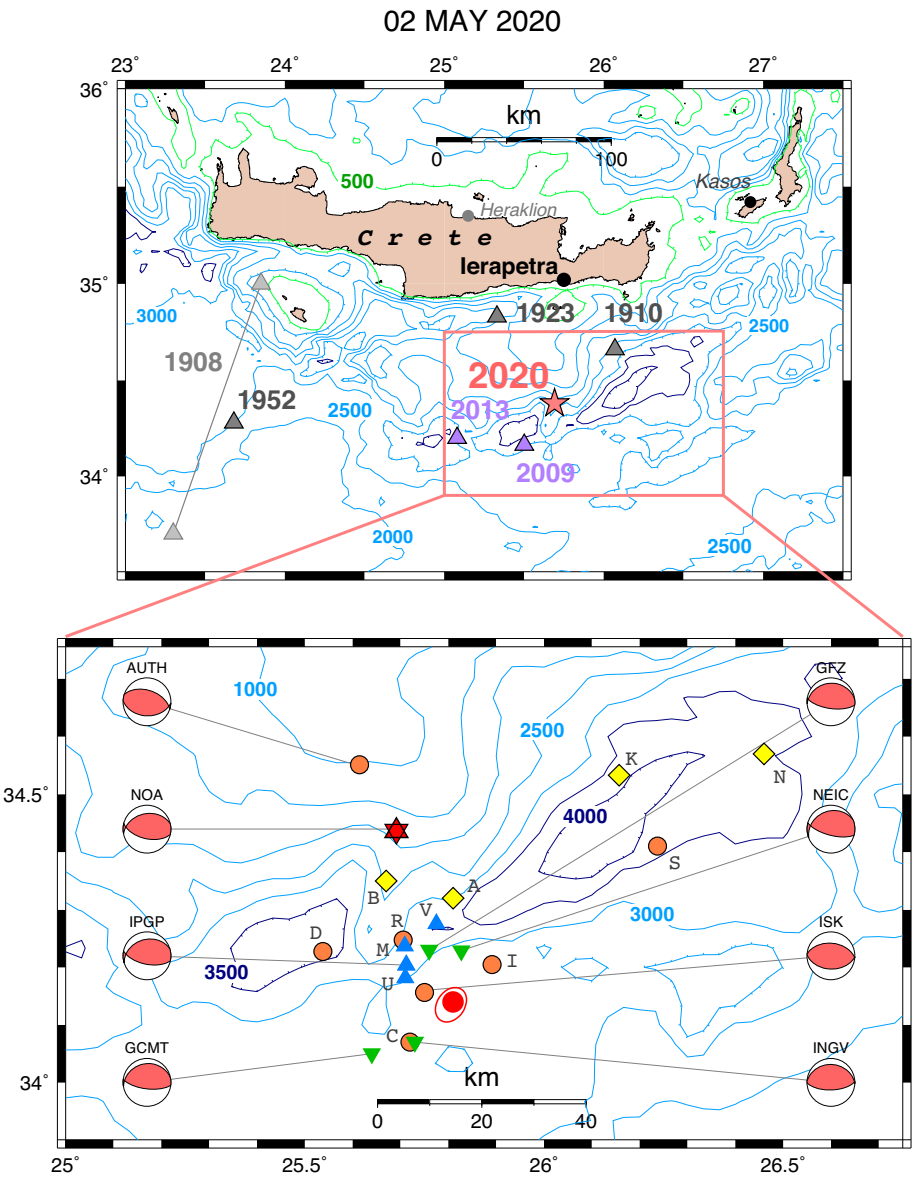

Figure 1. Location of the 2020 Ierapetra earthquake: Top: regional map showing NOA location (star), nearby 2009 and 2013 epicentres (purple triangles), and historical events discussed in Appendix B (grey triangles). Isobaths are shown at 500-m intervals (500 m: green, 1000–3000 m: light blue; 3500 m and deeper: dark blue). The filled circles identify the tide gauge stations at Heraklion, Ierapetra and Kasos. Bottom: close-up of the red box shown on top frame, with epicentres obtained by various agencies. Large red dot with confidence ellipse: relocation obtained in this study; blue triangles: solutions from worldwide centres (U: USGS-NEIC; M: Moscow and V: IDC-Vienna); orange dots: solutions from regional centres (C: CSEM; R: INGV, Rome; I: Geological Survey of Israel; S: San Fernando; D: Dubai); yellow diamonds: solutions from distant networks using local data (A: Australia, B: Beijing; K: Korea and N: Noumea). Also shown are the focal mechanisms obtained by CMT inversion (see the text for acronyms), with the corresponding centroids shown as downwards-pointing green inverted triangles (only when their location is inverted as part of the algorithm).

the Hellenic National Tsunami Warning Center of NOA), located approximately 60 km north of the epicentre (Fig. 1). The tsunami maximum (negative) amplitude was recorded 5 min after the arrival of the first peak. A weak recording of the tsunami was also observed at the NOA tide gauge station in Kasos Island (26.9217°E, 35.4188°N), 50 km east of Crete, but the wave amplitude was comparable to the noise level and thus the wave arrival could not be determined with high confidence, while the recording of the NOA tide gauge in Heraklion (25.1526°E, 35.3485°N), located in northern Crete, did not reveal any distinguishable waves (locations shown in Fig. 1).

Based on the location and magnitude of the earthquake, initial tsunami warning messages were disseminated by the Tsunami Service Providers (TSPs) that are monitoring the area (more information is provided in Appendix A). All TSPs disseminated their initial message, which was solely based on the earthquake magnitude, within 8–12 min after the earthquake. Following the detection of the tsunami at the tide gauge of Ierapetra, tsunami generation was confirmed by all three TSPs in their second (tsunami ongoing) message, which reported the measured wave height. The alert was lifted by all TSPs when the sea level oscillation became comparable to the background noise, ∼5 hr after the earthquake.

About ten years earlier, on 2009 July 1, a magnitude 6.45 earthquake ruptured a fault segment just west of the epicentre of the 2020 May 2 earthquake (Fig. 1) triggering a small tsunami (Ta Nea 2009; Ambraseys & Synolakis 2010; Bocchini *et al.* 2020), but no tide gauge recording of the generated tsunami is available. While tsunamis of small amplitudes (<0.5 m) do not cause extensive coastal flooding, tsunami-induced currents can be potentially hazardous for navigation in the near-shore, particularly near topographic features (such as breakwaters or headlands) that force transverse velocity gradients and introduce horizontal vorticity in the flow (Lynett *et al.* 2014; Borrero *et al.* 2015; Kalligeris *et al.* 2016).

Sightings of such strong tsunami-induced currents in harbours near the earthquake epicentre were reported (along with video recordings) for the Crete 2009, Lesvos 2017 and Crete 2020 tsunami events, a testament that tsunamis of this size can cause disturbances for safe navigation around ports and harbours. In the summer of 2017, two other tsunamigenic earthquakes of similar magnitude impacted the SE Aegean region, an $M_w = 6.3$ south of Lesvos and an $M_w = 6.6$ between Kos and Bodrum. Maximum wave amplitude was estimated to be 0.3 m for Lesvos (Annunziato *et al.* 2017) and maximum wave runup was measured at 1.5–2 m for Bodrum-Kos (Dogan *et al.* 2019).

2 EARTHQUAKE RELOCATION AND FOCAL MECHANISM

2.1 Location

The 2020 Ierapetra earthquake was located by more than 20 agencies worldwide, with the results regrouped on the bottom frame of Fig. 1. The blue triangles are epicentres proposed by worldwide centres (e.g. USGS National Earthquake information Center [U], Institute of Earth Physics of Paris [IPGP], International Data Center, Vienna [V]; note that as of the day of writing, 2022 February 03 12:07:55, the International Seismological Center [ISC] location is not yet available), the orange dots are solutions obtained by regional networks (e.g. Kandilli Observatory, Istanbul [ISK], Geophysical Institute of Israel [I], GII), and the yellow diamonds by more distant centres (e.g. Geoscience Australia [A], KEA). The green inverted triangles are centroids obtained by moment tensor inversions (e.g. GlobalCMT [GCMT], German Research Centre for Geosciences [GFZ]). The red star is the epicentral solution (34.44°N; 25.69°E) obtained at the NOA using stations of the Hellenic Unified Seismological Network (HUSN). The red solid dot is a solution obtained from 165 worldwide arrival times listed (but not yet inverted) by the ISC, using the method of Wysession *et al.* (1991), which estimates a confidence ellipse (also shown) through a Monte Carlo algorithm injecting Gaussian noise (in this case with $\sigma_G = 1$ s) in the data set.

The NOA and AUTH (Aristotle University of Thessaloniki) epicenters are displaced North 22 and 35 km, respectively, from the cluster of worldwide solutions. This systematic bias probably stems from the use of the global *ak*135 model which overestimates regional velocities, resulting in underestimated model slownesses at constant distances, and in turn in underestimated distances for an observed slowness derived from a regional set of arrivals with little azimuthal coverage. This is also the case for solutions obtained by more distant regional centres (e.g. San Fernando, Spain [S]), which may suffer from a lack of azimuthal coverage, and from the use of a velocity model poorly adapted to the actual path sampled by the rays.

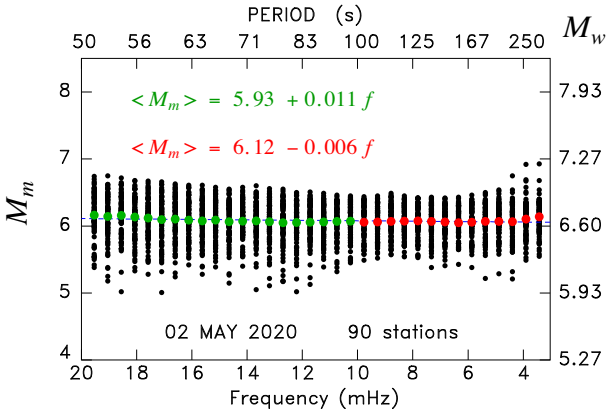

Figure 2. Mantle magnitude M_m (Okal & Talandier 1989) computed at 90 stations and 34 periods from 50 s (left) to 333 s (right), scaled linearly in frequency. The values are averaged over stations at each frequency and regressed separately below (red) and above (green) 10 mHz. Note the exceptional stability of the averages, indicating the absence of an anomalous (slow or fast) trend in the source spectrum.

The NOA solution yields a hypocentral depth of 9 ± 4 km. Locations from other agencies (when not constrained) are generally consistent, with depths ranging from 10.6 to 17 km. As part of our focal mechanism inversion, we obtained a centroid depth of 16 km.

In conclusion, most solutions are within 20 km of the Hellenic Arc trench, as identified by the isobath contours in Fig. 1, indicating that this shallow earthquake expresses subduction of the Nubia plate under the Aegean arc.

2.2 Focal mechanism and moment

Moment tensor solutions for the 2020 Ierapetra earthquake have been published by a number of agencies, and are displayed on Fig. 1. The solution at the NOA was obtained by inversion of three-component seismograms at 15 stations of the HUSN. The algorithm leaves the latitude and longitude of the centroid fixed, but inverts for its depth, as well as for the five deviatoric components of the moment tensor. This yielded a centroid depth of 16 km, and a best double-couple oriented ($\phi = 258°$; $\delta = 36°$; $\lambda = 69°$), with $M_0 = 9.98 \times 10^{18}$ N·m. The other solutions shown on Fig. 1 are essentially identical to NOA's, being rotated from it 17.5° ± 5.5° in the formalism of Kagan (1991), out of a theoretical maximum of 120°. On the other hand, we note that the NEIC W-phase solution has a smaller moment of only 6.05×10^{18} N·m, and the AUTH one a significantly deficient moment, at 3.5×10^{18} N·m.

2.3 Absence of trends in source spectrum

We analysed records of the 2020 Ierapetra earthquake for any possible anomalous trends in the source spectrum. We first computed mantle magnitudes from long-period Rayleigh waves at 90 stations of the Global Seismic Network, following a technique adapted from Okal (2013). On Fig. 2, we show the evolution of the mantle magnitude M_m with period (increasing to the right). The results are remarkably constant, and, in particular, feature no increase at the lower frequencies ($f < 10$ mHz; in red) as compared to the higher ones ($f > 10$ mHz; in green); such an increase would be typical of slowness in the source.

Next, we computed an energy-to-moment ratio, following the technique of Newman & Okal (1998). As shown on Fig. 3, we

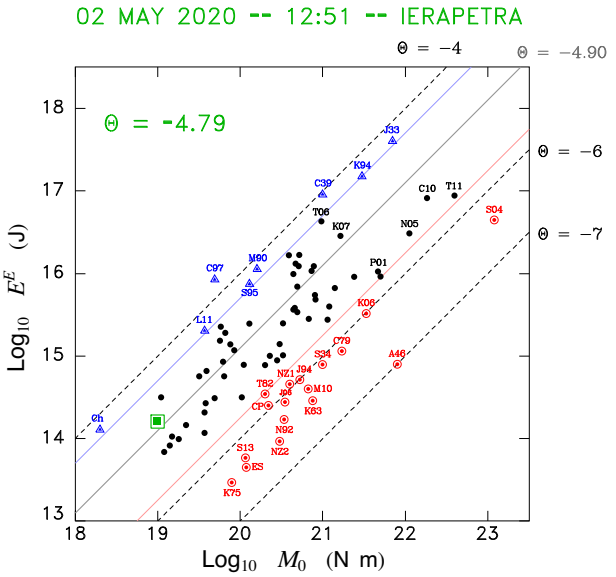

Figure 3. Energy-to-moment ratio computed for the 2020 Ierapetra earthquake (green centred square) in the formalism of Newman & Okal (1998). In this logarithmic plot, oblique lines feature constant values of the slowness parameter Θ. The value is compared to a background of large earthquakes of the past few decades; Slow events ($\Theta \leq -5.8$), such as tsunami earthquakes, are shown as red bull's eye symbols, fast or 'snappy' events as blue triangles; see Okal & Saloor (2017, fig. 13) for a complete list of outlined events.

find a slowness parameter relating estimated radiated energy E^E to seismic moment M_0, ($\Theta = \log_{10}E^E/M_0 = -4.79$) in excellent agreement with the average value (-4.90) expected theoretically and observed experimentally. We conclude that the earthquake's source spectrum is neither slow nor fast. While this result may appear banal, it constitutes a necessary step in justifying the use of scaling laws to compute static displacements as initial conditions for tsunami simulations.

2.4 Significant events in background seismicity

In modern times, the epicentre of the slightly smaller earthquake ($M_0 = 5.8 \times 10^{18}$ N·m; $M_w = 6.45$) that occurred on 2009 July 01, is located 52 km Southwest of our 2020 epicentre. Another, even smaller, earthquake took place slightly farther West, on 2013 June 15, without any reported tsunami. Both of these shocks, shown on Fig. 1, feature shallow angle thrust mechanisms, rotated from our 2020 solution only 22° and 29°, respectively, in the formalism of Kagan (1991). Neither of them feature an anomalous source spectrum, with parameters $\Theta = -5.03$ (2009) and -5.04 (2013).

The study area shown on Fig. 1 was also the site of historical seismicity, as discussed in Appendix B. None of those older earthquakes resulted in reported tsunamis on the southern coast of Crete.

3 POST-TSUNAMI RECONNAISSANCE

A team of five scientists was deployed in the field three days after the earthquake to collect eyewitness descriptions and quantitative measurements of the tsunami effects, per standard methods (Synolakis & Okal 2005). The equipment and methods used in the field survey are described in Appendix C. All elevations reported in this manuscript were translated to the sea level at the time of the earthquake using the tide gauge data in Ierapetra.

3.1 Field survey main findings

The coastal sites shown in Fig. 4 were visited during the two-day reconnaissance survey. The quantitative measurements are summarized in Fig. 4 and Table A1 in Appendix D. A description of the main field survey findings is provided here, while a detailed description of each site visit is provided in Appendix D.

A ∼62 km coastal stretch between Tsoutsouros and Makry Gialos was surveyed along the south coast of Crete. Sightings of the tsunami in Tsoutsouros, Karstri, Arvi and Ierapetra were limited to observations in local harbours, where maximum wave runup did not exceed 0.90 m, and a 0.35 m wave runup was observed on a local beach in Makry Gialos. Given that the wave amplitude along the coast was below 1 m, the tsunami-induced currents observed inside the harbour basins were more noteworthy than the water level fluctuations. While some boats touched the seafloor during the drawdown phase, no damage to boats or coastal infrastructure was reported as a result of the tsunami. Most eyewitnesses described a leading-depression wave, at least six repetitions (waves), with the second wave being the largest.

The post-reconnaissance team also visited the island of Chrisi, which is located ∼14 km south of the town of Ierapetra and is the nearest coastal location to the epicentre of the 2020 May 2 earthquake. Two data points were collected, one on the south coast (0.61 m wave runup) and one on the north (0.95 m wave runup and −0.87 m wave drawdown), the runup point on the north coast being the largest measured in the survey.

The eyewitness interviews showed that most local residents in locations we visited unfortunately stayed near the coast to observe and film the unusual behaviour of the sea, while fewer reported that they moved to higher ground. The earthquake shaking along the coast of south Crete was reported as long-lasting but weak and was not felt by all eyewitness we interviewed, with some eyewitnesses not being able to immediately associate the unusual sea behaviour to an earthquake. However, local residents had also witnessed the small tsunami generated by the 2009 July 1 earthquake, and some eyewitnesses admitted that they had made the association to the earthquake, but nevertheless decided to stay near the coast.

The national tsunami warning message was received in the local administrative capital of Ierapetra, where Coast Guard officers asked local fishermen working on their boats to move away from the coast. We found no evidence of the tsunami warning reaching other coastal locations.

4 TIDE GAUGE RECORDING ANALYSIS

In 2015 December, the NOA installed a tide gauge near the entrance of the Ierapetra harbour for tsunami detection and to support the operations of the Hellenic National Tsunami Warning Center. It is a Datamar Geonica radar-type tide gauge (GEONICA 2015) that transmits data every 1 min in real time—the station samples every 1 s and each transmitted value corresponds to a 1 min average (of 60 samples), timestamped at the end of the sampling period. The tide gauge recording confirmed the generation of the tsunami and prompted the TSPs of NEAMTWS (see Appendix A for acronym) to issue tsunami ongoing messages.

The tsunami traveltimes (TTTs) in the eastern Mediterranean for the 2020 May 2 event are shown in Fig. 5 through tsunami rays originating from the earthquake epicentre; the rays were computed using the ray equations of Jobert & Jobert (1983), solved through the procedure outlined in Woods & Okal (1987) using the Etopo 2-arcmin grid, smoothed to satisfy the short wavelength condition

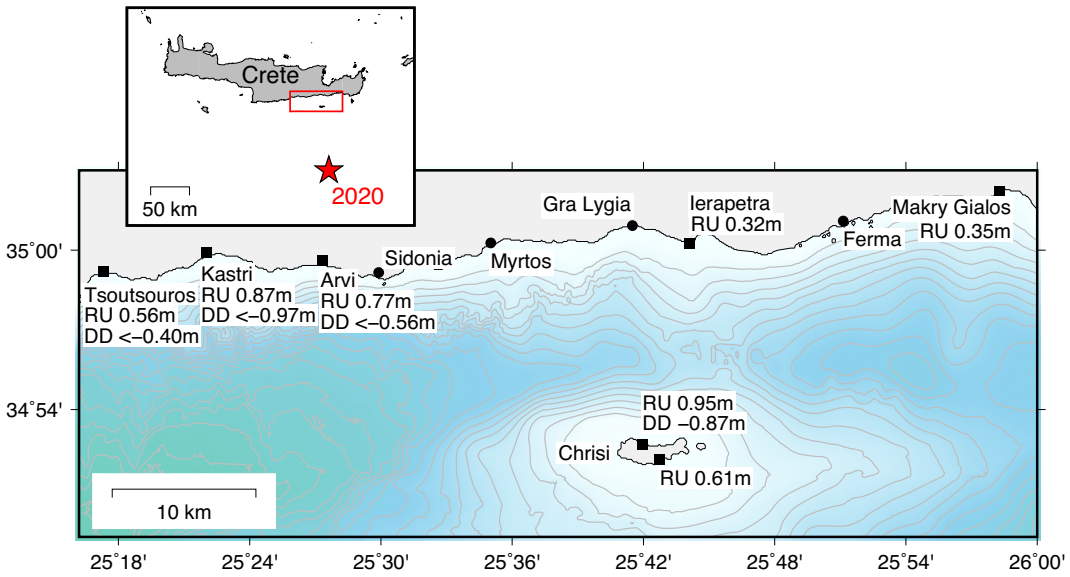

Figure 4. Locations in south Crete and Chrisi visited in the post-tsunami field survey. Locations where tsunami runup was measured are shown with the black squares. Runup (RU) and drawdown (DD) measurements are noted below the name of the coastal location. Locations visited where tsunami runup was not observed are shown with the black circles. EMODNET bathymetry contours drawn every 100 m. Figure inset shows the location of the field survey area relative to Crete and the earthquake epicentre.

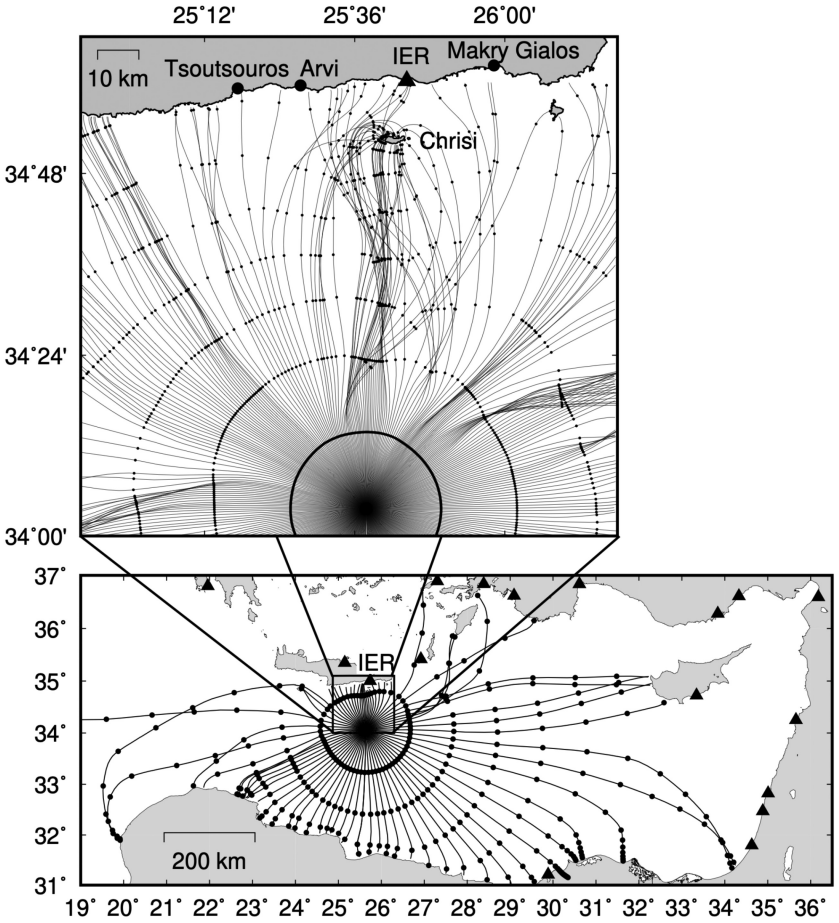

Figure 5. Direction of wave energy propagation for a point source positioned at the centroid of the the GCMT moment tensor (Fig. 1 and Table 1), presented through ray tracing. Rays are plotted at 1° and 5° increments, and dots denote arrival time plotted at 2 and 10 min increments in the top and bottom plots, respectively. Triangles show the locations of tide gauges that were transmitting real-time water level data to the IOC Sea Level Monitoring Facility at the time of the tsunami event, including the Ierapetra tide gauge (IER).

(Aki & Richards 1980; Satake 1988), and the linear dispersive equation to calculate wave celerity for a 3.7 min wave period. TTTs show that the tsunami waves reach the coast of south Crete within 10–20 min after the earthquake, the coast of Libya within ∼40 min and the western coast of Cyprus within ∼1 hr. Such arrival times allow limited time for effective tsunami warning and evacuation of the population. Tsunami detection in the NEAMTWS is heavily dependent on tide gauge recordings, making the density and distribution of tide gauges in the region a critical parameter for effective detection and alerting. Moreover, for small-amplitude tsunami events, near-field tide gauges are required to effectively record the generated tsunami before wave energy is attenuated, reaching background noise levels. The density of the rays, which can be translated to wave amplitude (Woods & Okal 1987), shows that bathymetry (without taking into account the source directivity, e.g. Okal & Synolakis, 2008) guides the main wave energy towards the southeast coastline of Crete and Chrisi (Fig. 5). Thus, the Ierapetra tide gauge was at an optimal geographical location for the detection of the May 2 tsunami and the tide gauge record provides an opportunity to study the generated tsunami.

The tidal signal of the tide gauge recording was obtained using a low-pass first-order Butterworth filter with a 90 min cutoff period (Figs 6 a and b). The spectral progression of the residual signal before and after the arrival of the tsunami was examined by applying the wavelet package of Torrence & Compo (1998), using the Morlet basis function with 26 scales of 1/4 spacing and wavenumber equal to 6. The wavelet analysis (Figs 6c and d) shows that the background noise prior to the arrival of the tsunami waves is well constrained in the period band between 7–12 min, with a predominant period at 9.5 min. The wave arrival initially shifts the spectral energy to the 2–6 min period range (centred at 3.6 min) and at later times, spectral energy is again generated in the 7–12 min range, which becomes the dominant energy band.

The spectral properties of the tsunami recording were also examined using the Welch (1967) averaged modified-periodogram technique which is non-time-dependent. The periodograms of the background and tsunami signal were computed on 6-hr segments of the unfiltered tide gauge recording before and after the first wave arrival, respectively. Each signal was divided into segments of 90 min, a 50 per cent overlap was applied between successive segments (Heidarzadeh *et al.* 2017), and each segment was tapered using a Hamming window. The periodogram plotted in Fig. 7(a) shows that the energy is contained in discrete frequency bands, before and after the arrival of the tsunami. The energy peak at 9.5 min is a distinct feature of both the background and tsunami time-series, and thus precludes this frequency band corresponding to the forcing system, but instead to the natural frequency of the forced system. The ratio of the two periodograms was also computed to identify the functional characteristics of the source (Rabinovich 1997). Fig. 7(b) shows that the tsunami energy lies between 2 and 23 min and is more pronounced in the range between 2 and 7 min. In combination with the wavelet analysis, it can be deduced that the initial tsunami forcing lies in the spectral range between 2 and 5 min, and that the energy in longer periods is the result of the excitation of resonant modes of the forced system. The resonant frequencies of the system are examined through numerical modelling in Section 5.3.

5 NUMERICAL MODELLING

The event was simulated using hydrodynamic models in order to infer the source of the tsunami and obtain a better understanding of the arrival time sequence in the study area. Two hydrodynamic models were used for this purpose, MOST (Titov & Synolakis 1998) and COULWAVE (Lynett *et al.* 2002). Both have been fully validated as per international protocols.

MOST (Method Of Splitting Tsunamis) is a model that solves the nonlinear shallow-water (depth-averaged) equations using the method of alternate steps and a finite-difference scheme (Titov & Synolakis 1995, 1998; Titov *et al.* 2016). The model inherently simulates wave nonlinearity and it allows to define telescopic relief grids of increasing resolution to account for wave shoaling and increased nonlinearity as the waves move from deeper to shallower water. COULWAVE is a long- and intermediate-wave modelling package that solves different approximations of the parent equations of motion. For this application, we use the fully nonlinear and mildly dispersive Boussinesq-type equations described in Kim *et al.* (2009).

MOST being a shallow-water model does not account for frequency dispersion through its governing equations, but has (limited) numerical dispersion properties through its numerical scheme (Burwell *et al.* 2007). On the other hand, the COULWAVE solver used here is weakly dispersive and models linear dispersion accurately up to $kh \approx 3$ (Nwogu 1993), where k is the wavenumber ($k = 2\pi/L$, where L is the wave length) and h is the local water depth. Due to the short wave periods generated by this earthquake and the relatively large water depths in the source region reaching values of ∼4.5 km (in the trenches of the Hellenic arc), it is useful to examine the effect of frequency dispersion by comparing the free surface results of the two models.

Numerical grids used with the models are described in Appendix F. MOST simulations using three nested grids (A–C) are labelled MOST-3G, and MOST simulations using all four nested grids (A–D) are labelled MOST-4G. Numerical simulations with COULWAVE, simply labelled COUL, use a single grid of 30 m cell size. The 30 m numerical grid adequately resolves the ∼20 m-wide Ierapetra harbour breakwater, using at least one grid point to represent the breakwater along its span.

5.1 Initial conditions—seismic sources

The earthquake sources considered in the hydrodynamic simulations are listed and described in Table 1. We have selected the north-dipping, low-angle plane of the published moment tensor solutions, as it is the most appropriate choice for the seismotectonic setting that dominates the study area. The fault rupture area and width corresponding to the moment magnitude of each source was inferred using the Wells & Coppersmith (1994) empirical relations for thrust faulting and slip magnitude was computed from the seismic moment using a modulus of elasticity equal to 35 GPa—note that the chosen source parameters have a small deviation from the Wells & Coppersmith (1994) scaling to test different slip magnitudes. The co-seismic deformation of the seafloor was computed using the Okada (1985) analytical formulae and the deformation was directly translated to the free surface as static initial conditions for the hydrodynamic simulations (Derakhti *et al.* 2019).

5.2 Numerical modelling results

The numerical simulation results for all initial conditions considered (Figs 8a–c) were evaluated by comparing the numerical mareograms corresponding to each source with the Ierapetra tide gauge record (Figs 8d–i). The numerical time-series at the model output rate (5 s,

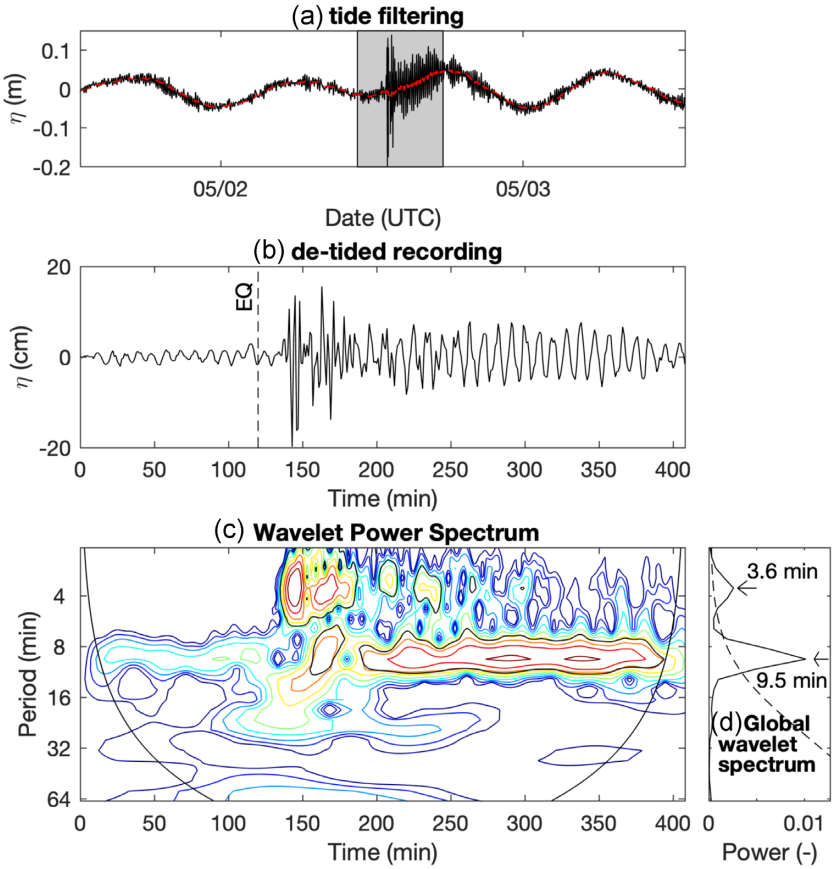

Figure 6. (a) The original tide gauge recording in Ierapetra (black line) and the low-pass filter representation of the tide (red line). (b) The residual signal after filtering the tide. (c) The wavelet power spectrum using the Morlet wavelet. (d) The global wavelet spectrum.

for both the MOST and COULWAVE simulations) were averaged within 1-min time windows to produce time-series compatible with the tide gauge record. The numerical time-series are presented both at the model output rate, and using the 1-min averaging.

The MOST-3G numerical mareogram for the USGS source shows an early tsunami arrival time (∼1.8 min) at the tide gauge compared to the recording (Fig. 8d), meaning that the source is located too far north. Also, the source based on the relocated coordinates of this study and the NOA CMT produces an earlier-than-observed wave arrival time at the tide gauge (Figs 8 h–i).

The GCMT source, on the other hand, produces mareograms that compare well both to the amplitude and the phasing of the first three waves recorded by the tide gauge. The 1-min average mareogram of the MOST-3G simulation matches the amplitude and phase of the two leading waves better (Fig. 8f), whereas the 1-min average mareogram of the COUL simulation matches the phase and amplitude of the following two (main) waves better (Fig. 8g). The first wave, however, should be treated with caution, since its amplitude is comparable to the background noise level of the tide gauge recording. With respect to the effect of frequency dispersion, the COUL simulation produces slightly higher amplitudes compared to the MOST-3G simulation, whereas the main effect is the later arrival of the waves in the COUL simulation (Fig. 8e); the average arrival time difference for the first three peaks between the MOST-3G and COUL simulations is ∼36 s. This time difference is in agreement with the arrival time difference computed by applying the linear phase speed for a wave with 2.9 min period and the shallow-water speed over the shortest wave ray between the GCMT centroid and Ierapetra that passes by the east side of Chrisi island (Fig. 8b). At the source region, where the water depth is ∼2.7 km, a 36 s difference in arrival time for a 2.9 min period wave translates to a ∼5.5 km difference in source location.

Figs 9(a)–(d) show 2-D snapshots of wave amplitude as the tsunami arrives in the study area, extracted by the COUL simulation using the GCMT source. Figs 9(a) and (b) correspond to the time when the leading-depression wave arrives in Ierapetra from the east and west sides of the island of Chrisi, respectively. Fig. 9(b) also shows that the elevation wave has just reached the south coast of Chrisi, Tsoutsouros, Kastri, Arvi and Makry Gialos. Figs 9(c) and (d) show how the wave wraps around the island of Chrisi, with the two wave fronts merging on the back side of the island. The merging of the wave fronts on the lee side of the island of Chrisi is also visible in the tsunami ray plot of Fig. 5. While ray theory only accounts for refraction (and not diffraction), it provides an elementary explanation of how wave rays with length comparable to the diameter of the island meet on the lee side of the island. Wind-generated waves with shorter wavelengths are less sensitive to bathymetry and thus are refracted less efficiently around the island, creating a shadow zone on the lee side (e.g. Niu 2021, and references therein). By contrast, long waves such as tsunamis can wrap around the island, leading to a perhaps counter-intuitive phenomenon, first noted at Babi island, Indonesia, during the field survey of the 1992 Flores tsunami (Yeh *et al.* 1993), and later studied through lab experiments (Liu *et al.* 1995; Briggs *et al.* 1995), analytically (Kânoğlu *et al.* 1998) and through numerical simulations (Titov & Synolakis 1998). This wrap-around effect and the

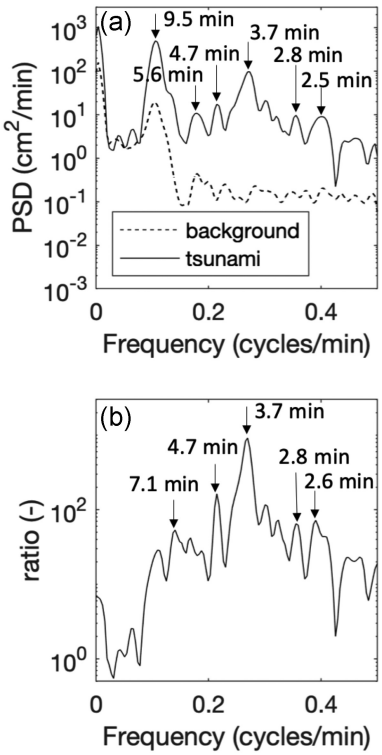

Figure 7. (a) The periodograms of the background and tsunami signals. (b) The ratio of the two periodograms (tsunami/background). Averaging of four overlapping segments corresponds to ∼8 degrees of freedom, and PSD 95 per cent lower and upper confidence interval factors are 0.46 and 3.67, respectively.

merging of the two wave fronts approaching from each side of the island likely produced the enhanced wave runup of the north side of Chrisi, where the maximum runup was recorded in the field survey.

The wave sequence in north Chrisi extracted from the COUL simulation (Fig. 9f) features a small-amplitude leading-depression, a small rise, another small water level drop and rise, before the main depression wave and flood arrive. The timing and amplitude of the main depression wave matches the water level drop in the local harbour extracted from the timestamped eyewitness pictures (Figs A8f and g); the eyewitness described the first depression as the largest, however, the previous two small-amplitude waves could have gone unnoted. The numerical mareogram from Arvi (Fig. 9e), shows a small-amplitude leading-depression and three main waves following. The numerical mareogram amplitude of the fourth trough in Arvi matches the water levels inferred from the first eyewitness video (Figs A8a–c), but arrives 28 s later than the minimum water level extracted from the video. The simulation suggests that the third crest is the largest, but comparable to the second which was described as the largest by the eyewitnesses in Arvi. The water levels extracted from the second eyewitness video in Arvi (Figs A8d and e) appear to correspond to waves beyond the first three and the modelled amplitudes are deficient compared to the observations. However, nested grids of higher resolution that resolve the harbour geometry were not used, and thus the harbour basin response was not accurately modelled.

The maximum wave amplitude map extracted from the COUL simulation (Fig. 9g) shows that the wave energy was directed from the source primarily towards the island of Chrisi and the coastline stretch between Tsoutsouros and Ierapetra. The maximum wave amplitude starts decaying to the east of Ierapetra, with Makry Gialos receiving the least wave energy from all the coastal locations visited. These observations are generally in agreement with the field measurements of wave runup. However, the runup data points are not directly comparable, since the harbour basin response could have affected the runup data points collected inside harbours, and thus clear conclusions cannot be drawn on the accuracy of the model results in locations other than Ierapetra where the nearshore bathymetry and the harbour geometry were resolved in the COUL simulation.

5.3 Tide gauge response—natural frequencies of the system

In this section, we analyse the oscillations recorded at the Ierapetra tide gauge before and after the arrival of the tsunami. As shown in Section 4, the background noise prior to the arrival of the tsunami oscillates in the 7–12 min period range. Following the arrival of the tsunami, the predominant energy temporarily shifts to the 2–6 min period range, interpreted as the frequency range of the tsunami source, and ∼1 hr later returns to the 7–12 min period range. This narrow-frequency band, which dominated the spectrum prior to the earthquake, and was excited to larger amplitudes by the tsunami, can be interpreted as the natural frequency band of the system.

The tide gauge is located at the edge of the external breakwater, outside the harbour basin. Therefore, it is unlikely that the harbour basin response to external forcing (storm waves, swell, tsunamis, etc.) will lead to significant wave amplification at the harbour basin's natural oscillation frequencies in the particular deployment location. Nevertheless, we first explored the harbour's response to this tsunami event by analysing the time-series of free surface elevation inside the harbour basin. A numerical grid with 2 m cell size, focusing only on the harbour of Ierapetra was created for this purpose. A 3 hr MOST-4G simulation using the GCMT source and four nested grids (grids A, B, C and D shown in Fig. A10 of Appendix F) yielded the time-series of free surface elevation. The first hour of simulation that includes the tsunami signal was discarded, and the time-series of the last two hours of simulation were analysed through Fast Fourier Transform analysis.

The resulting wave power spectra $S_i(f)$ corresponding to each node i out of the $N = 8199$ nodes inside the harbour basin were averaged (see Fig. A10 for the region over which the free surface elevation time-series inside the harbour were averaged) to obtain the space-averaged power spectrum $\bar{S}(f)$ defined as (Maravelakis *et al.* 2021)

$$\bar{S}(f) = \frac{1}{N}\sum_{i=1}^{N} S_i(f). \quad (1)$$

The space-averaged spectrum shown in Fig. 10(a) features distinct peaks at the frequency bins that contain the most energy; plotting the spectral energy distribution corresponding to each of these peaks reveals the modes of the system. Starting with the lower frequencies, the most prominent peaks correspond to periods of 8.1 and 5.4 min. These are followed by peaks at 4.5, 3.7, 3.3 and 2.9 min. The harbour modes of these low-frequency oscillations share the same pattern featuring a decaying energy distribution from west to east (Fig. 10c). Only the highest frequency peak of 2.4 min period corresponds to a harbour basin mode, and Fig. 10(c) reveals that it is the Helmholtz mode for an open-ended basin (Rabinovich 2009). Plotting the mode corresponding to the 1.3 min peak reveals the distinctive second harbour basin mode (fundamental mode for a closed basin) with

Table 1. Earthquake source parameters used in the hydrodynamic simulations. The coordinates, with the exception of the NOA source, correspond to the centroid of the moment tensor solutions and were set as the centre of the fault-rupture area, L, W correspond to the fault rupture length and width, respectively, depth corresponds to the centroid of the moment tensors and was set as the mid-depth value of the fault rupture area, and Δu corresponds to the slip magnitude. The coded NOA—this study source uses the relocated coordinates of this study and the NOA CMT.

Institute/ name	Seismic moment (N·m)	Lat (°N)	Lon (°E)	Depth (km)	Strike (°)	Dip (°)	Rake (°)	L (km)	W (km)	Δu (m)
USGS	8.022×10^{18}	34.184	25.714	11.5	229	31	46	22.1	11.7	0.89
GCMT	1.02×10^{19}	34.06	25.63	12.0	257	24	71	24.1	12.5	0.96
NOA—this study	1.0×10^{19}	34.14	25.81	16.0	258	36	69	25.2	12.9	0.88

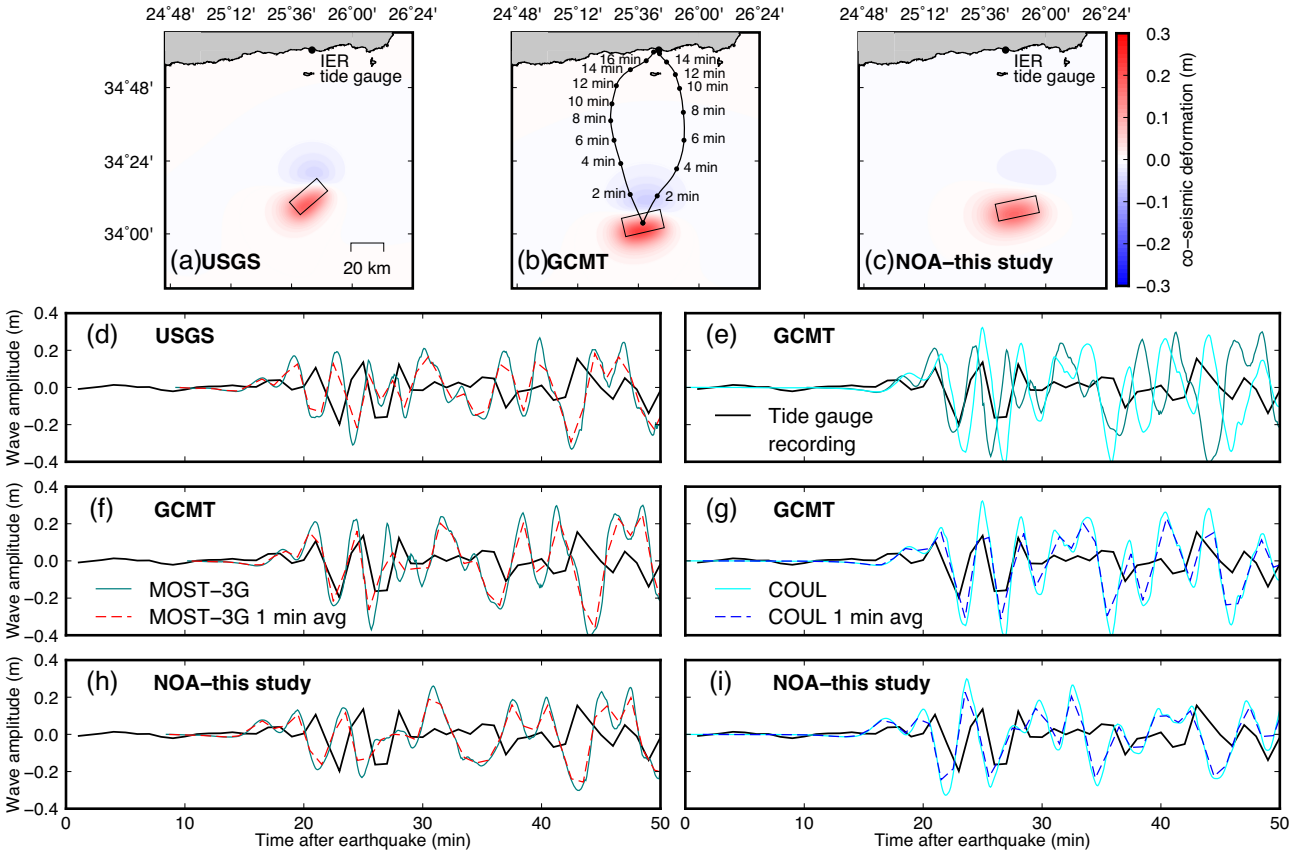

Figure 8. (a)–(c) The projected fault rupture areas (black rectangles) and the corresponding co-seismic vertical seafloor deformation (colour-coded shading) computed using the sources listed in Table 1. Subplot (b) also shows the shortest wave rays between the GCMT centroid and Ierapetra passing on either side of Chrisi; the circles denote wave traveltime on the rays with a 2 min spacing computed for a 2.9 min period wave. (d)–(i) Comparison between the (filtered) Ierapetra tide gauge recording and the numerical time-series extracted from the MOST-3G and COUL simulations corresponding to the sources listed in Table 1; continuous lines correspond to the unprocessed time-series extracted from the models, and the dashed lines correspond to 1-min averaged values (see the text for more details).

two antinodes at the west and east basin extremes, and a node running across the middle section of the basin (Fig. 10d). Thus, the spectral peaks at periods of oscillation longer than 2.4 min must belong to a larger scale system resonance mechanism, such as bay oscillations.

The same analysis was performed for time-series collected from the whole numerical domain of grid C (see Fig. A10 for the region over which the free surface elevation time-series of grid C were averaged). The space-averaged spectrum of grid C shown in Fig. 10(b) features the distinct peak at 7.9 min, which most likely corresponds to the 8.1 min resonant period identified through the harbour space-averaged spectrum. Plotting the spectral energy distribution corresponding to this peak (Fig. 10e) reveals that the mode involves the whole bay of Ierapetra, featuring an antinode along the coastline and progressively less energy to the south towards the continental shelf. This very energetic mode creates high amplitude oscillations inside the harbour basin. When multiple basins are connected, as in this case, the combined resonant mode, which may be dominated by the larger basin, can have a period greater than the Helmholtz mode of the smaller basin (Marcos *et al.* 2004; Vela *et al.* 2011). The resonant period and mode of 7.9 min revealed through numerical modelling could correspond to the 9.5 min period oscillation identified in the tide gauge record (Section 4), which dominated the spectral amplitudes both before and some time after the arrival of the tsunami (Fig. 6). Prior to the arrival of the tsunami, this bay

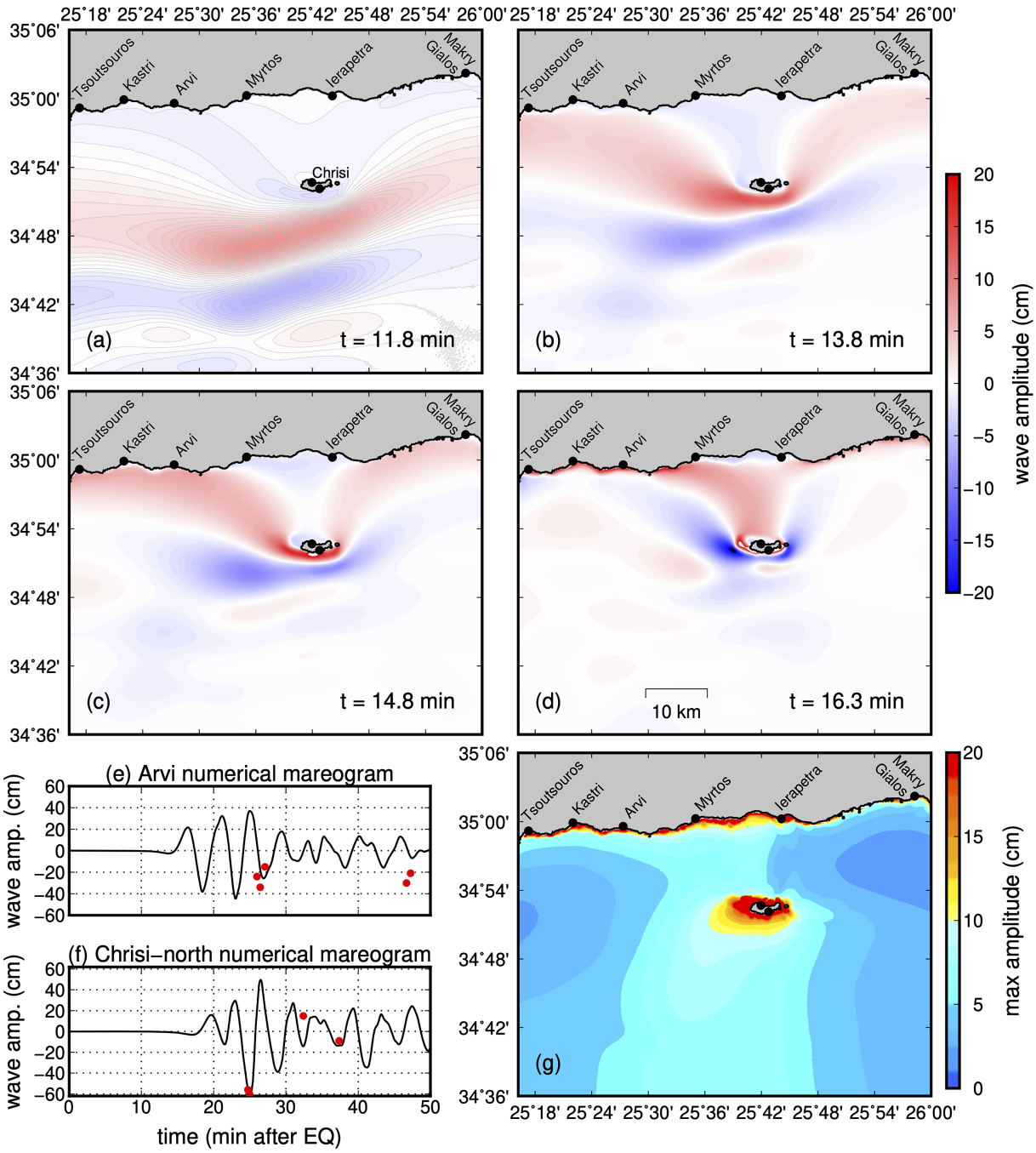

Figure 9. Results from the COUL simulation using the GCMT source. (a)–(d) Snapshots of wave amplitude with time stated in minutes after the earthquake. (e) and (f) Numerical mareograms from grid nodes just offshore Arvi and the north point of Chrisi, at water depths of 1.8 and 1.7 m, respectively; the red points correspond to water level data points extracted from the eyewitness pictures and videos shown in Fig. A8. (g) Maximum wave amplitude map.

mode must have been activated through swell due to strong western winds. The other spectral peaks of the grid C space-averaged spectrum correspond to higher modes of the two bays, west and east of the harbour (Figs 10f–h). The periodogram of the tide gauge signal (Fig. 7) features peaks close to all natural oscillation periods identified through the harbour and grid C space-averaged spectra.

6 DISCUSSION AND CONCLUSIONS

This study presents our findings for the $M_w = 6.6$ earthquake that occurred south of the coast of Crete, Greece, on 2020 May 2, and the small–amplitude tsunami that was generated. Our earthquake relocation suggests an epicentre solution of 34.14°N, 25.81°E (Fig. 1). The moment tensor inversion of the NOA yielded a centroid depth

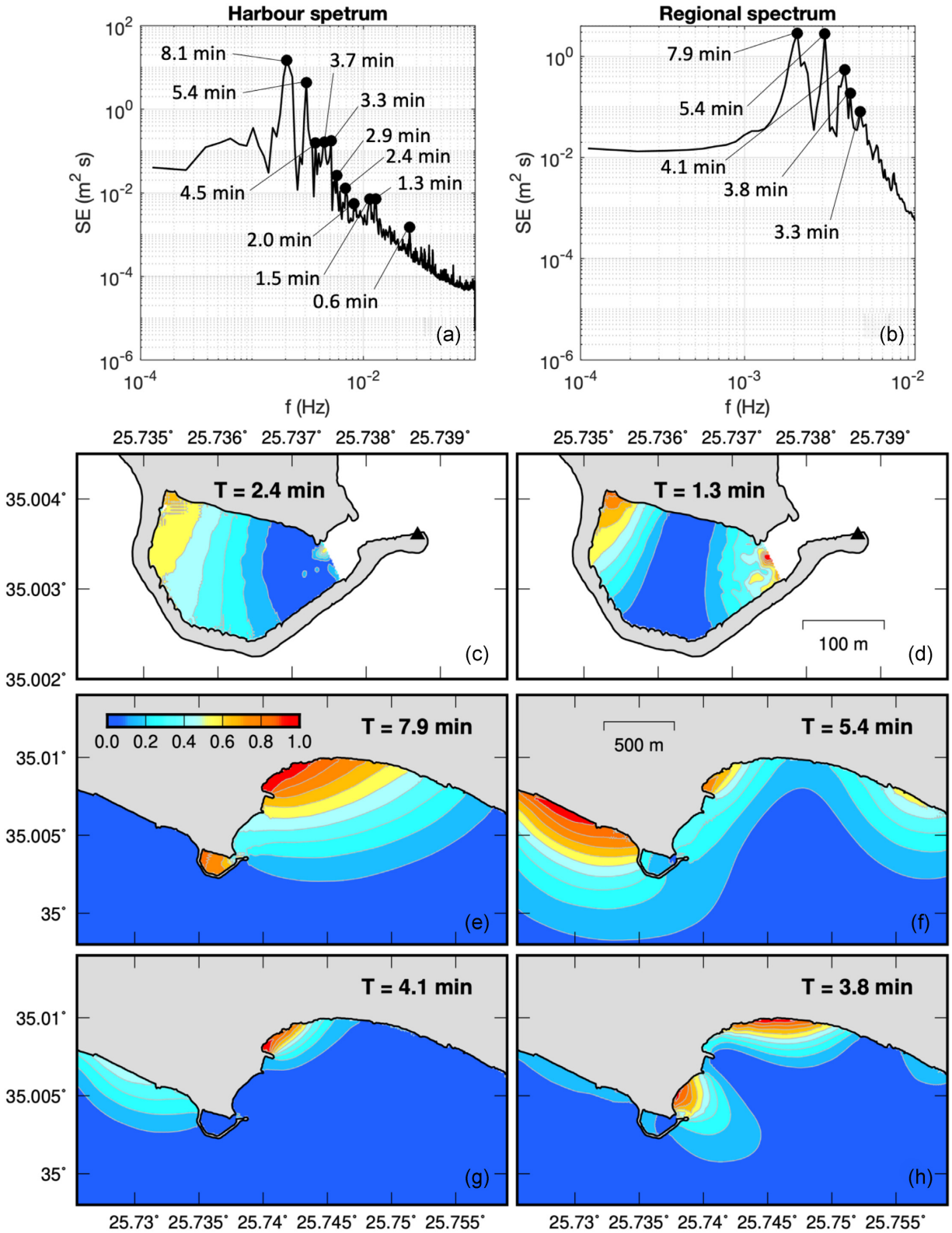

Figure 10. (a) and (b) The space-averaged spectra and (c)–(h) the natural modes of the system extracted from the MOST-4G numerical simulation. Subplots (c) and (d) correspond to the first two modes of the harbour basin and subplots (e)–(h) to the natural modes of the bay/continental shelf. The colourmap of each mode subplot has been normalized using the maximum value. The black triangles in subplots (c) and (d) denote the tide gauge location.

of 16 km, and a best double-couple oriented ($\phi = 258^\circ$; $\delta = 36^\circ$; $\lambda = 69^\circ$). The focal depth is consistent with other agencies in the range from 10.6 to 17 km. NOA's seismic moment of $M_0 = 9.98 \times 10^{18}$ N·m is consistent with most of the other agencies besides the NEIC W-phase solution, which has a smaller moment of only 6.05 $\times 10^{18}$ N·m, and the AUTH one which has a significantly deficient moment, at 3.5 $\times 10^{18}$ N·m.

We also analysed the earthquake to identify possible anomalous trends in the source spectrum. We found no increase in energy at the lower frequencies compared to the higher frequencies of the spectrum (Fig. 2), and the slowness parameter Θ (Newman & Okal 1998) was found to be in excellent agreement with the average value (Fig. 3). Thus, we conclude that the earthquake is neither slow nor fast, and that standard scaling laws are applicable when inferring the fault rupture area to generate the initial conditions for the tsunami simulations.

The earthquake generated a tsunami that was recorded by NOA's tide gauge in the harbour of Ierapetra, registering wave amplitudes up to ∼20 cm (Fig. 6). The tsunami recording served as a confirmation of tsunami generation, prompting TSPs operating in the eastern Mediterranean to issue tsunami ongoing messages. Following the confirmation of tsunami generation, a post-tsunami reconnaissance team was deployed in the field three days after the earthquake to collect eyewitness descriptions and quantitative measurements of the tsunami effects per standard methods.

Along the southern coast of Crete, between the coastal town and harbour of Makry Gialos on the east, and the coastal town and harbour of Tsoutsouros on the west, we measured wave runup values ranging between 0.35 and 0.87 m (Fig. 4 and Table A1). The tsunami-induced waves and currents were noted mostly inside harbours, with the exception of Makry Gialos, where an eyewitness observed the waves on a local beach. We also collected data points on the island of Chrisi, located ∼15 km south of the coast of Crete, both on the north and south sides of the island. On the southern coast of Chrisi, which was the coastal location first impacted by the tsunami, wave runup reached 0.61 m. On the northern coast of Chrisi, wave runup reached 0.95 m, the maximum measured in the survey, because the tsunami waves wrapped around the island and then merged on its lee (northern) side; this constitutes one more example of this counter-intuitive effect, where the lee side of the island, which could be expected to be sheltered from the incoming wave, is actually the site of the highest runup values. The eyewitness reports on the polarity generally suggest a leading-depression wave and a largest second wave. Valuable timestamped eyewitness pictures and videos collected from Arvi and the north coast of Chrisi were analysed to extract water levels that were used to validate the numerical modelling results (Fig. A8).

Numerical simulations were performed for two published moment tensor solutions, namely the USGS, GCMT and for the NOA moment tensor solution used with the relocated epicentre produced in this study. The fault rupture area and slip magnitude were determined using the Wells & Coppersmith (1994) empirical relations. Among the three sources considered, our numerical simulations showed that the GCMT model provided the best fit between simulated mareograms and the tide gauge recording at Ierapetra (Fig. 8). The amplitudes in the numerical mareograms closely matched the recorded values in Ierapetra (Figs 8 f–g) and had good agreement with the water levels extracted from the eyewitness videos and pictures in Arvi and the northern coast of Chrisi, respectively (Figs 9e and f), justifying the use of scaling laws to infer the source parameters, while also validating the analysis of the earthquake source spectrum.

As this tsunami was relatively small in wavelength, two numerical models were used to assess the importance of frequency dispersion: MOST, which solves the nonlinear shallow-water equations, and COULWAVE, solving Boussinesq-type hydrodynamic equations. The COULWAVE simulation using the GCMT source produced a numerical mareogram that has a phase shift (later arrival) compared to the mareogram produced through the MOST simulation (Fig. 8e). The phase shift translates to a ∼5.5 km difference in the epicentral region. The mareogram wave amplitudes yielded by the COULWAVE simulation were slightly higher for the first four waves compared to the MOST-extracted numerical mareogram using the GCMT source. This observation is attributed mostly to frequency dispersion, and to a lesser degree to differences in the initialization of the simulations due to COULWAVE solving higher order derivatives compared to MOST. Significant differences between the two mareograms were observed for the fourth wave and beyond, with the one-way coupling boundary conditions used in the grid nesting of the MOST simulation possibly playing a role. The overall significance of frequency dispersion is deemed low for this tsunami event, at least for the distance between the source and site (∼105 km for the GCMT epicentre) and regional water depths considered. Based on the inter-model comparison, the shallow-water model performance is deemed adequate to model this tsunami event, at least for the distances considered in this study. While there is dispersive energy in the tsunami, due to the relatively short travel distance these dispersive effects do not significantly modify the wave form, or the leading wave arrival time. Therefore, the shallow water equations in the case of this tsunami can be used both for assessing the impact of the tsunami, but also to infer the source of the tsunami based on the tide gauge recording.

Spectral analysis of the Ierapetra tide gauge recording showed that the tsunami wave energy was contained in the 2–5 min period range (Fig. 6). A background noise in the 7–12 min period band of the signal, peaking at 9.5 min is distinguishable prior to the arrival of the waves, and becomes more pronounced ∼1 hr after first wave arrival. A high-resolution numerical simulation using the GCMT source revealed an energetic mode of the Ierapetra bay at a resonant period of ∼7.9 min (Fig. 10). While it does not match the 9.5 min produced through spectral analysis of the recording, perhaps due to inaccuracies in the bathymetry used in the simulation, this energetic resonant mode of the bay is most likely responsible for the background noise found in the tide gauge signal and for the slow decay of the recorded wave amplitudes following the arrival of the tsunami in Ierapetra. This is another reminder that tsunamis excite bays and harbours that can be left oscillating at their own frequencies for several hours after the initial arrival of the tsunami, a situation which should be taken into account by Civil Defence authorities for the purpose of issuing an all clear.

Even through no damage was reported, this tsunami event serves as a reminder of the tsunami-generation potential of earthquakes occurring along the Hellenic Arc. The Hellenic Arc has produced the largest known earthquake-generated tsunamis in the eastern Mediterranean, namely the 365 and 1303 AD tsunamis. A review of four historical submarine earthquakes that have occurred south of Crete presented in Appendix B reveals the return period of earthquakes with M∼6.5 in a region that is believed to be capable of producing M8 earthquakes (e.g. Valle *et al.*, 2014; England *et al.*, 2015).

People staying near the coast to film the tsunami-induced currents on 2020 May 2 is discouraging, given the extensive referencing of

such dangerous practices in the literature (Kânoğlu *et al.* 2015; Okal 2015, and references therein). It also highlights the urgent need to raise tsunami awareness in the region. The behaviour of witnesses can surely be considered careless by not evacuating more proactively. In the case of locations with physical infrastructure, where nonlinear effects and strong currents may be expected (e.g. harbours and marinas), systematic deployments of time-lapse cameras (e.g. Winterl *et al.*, 2020) could be very valuable for both tsunami warning operations and for future research.

ACKNOWLEDGMENTS

The authors would like to acknowledge the support of the General Secretariat of Civil Protection, Greece that made the field trip possible during the COVID-19 lockdown, as well as the hospitality and support of the Municipality of Ierapetra that organized our transportation to the island of Chrisi under difficult circumstances. Last, the authors want to thank the Hydrographic Service of Greece that provided an updated bathymetric DEM for our high-resolution hydrodynamic simulations around the harbour of Ierapetra. The paper was improved by constructive reviews.

DATA AVAILABILITY

The data underlying this paper will be shared on reasonable request to the corresponding author.

REFERENCES

Agisoft, L.L.C., 2016. *Agisoft PhotoScan Professional v. 1.2. 4,* AgiSoft L.L.C., St. Petersburg, Russia.

Aki, K. & Richards, P.G., 1980. *Quantitative Seismology,* W. H. Freeman, San Francisco.

Ambraseys, N. & Synolakis, C.E., 2010. Tsunami catalogs for the Eastern Mediterranean, revisited, *J. Earthq. Eng.,* **14**(3), 309–330.

Annunziato, A., Papadopoulos, G.A., Yalciner, A. *et al.*, 2017. *Analysis of the Tsunami Event caused by the Mw 6.3 Lesvos Island (East Aegean Sea) Earthquake of 12th June 2017, Joint Research Centre Report,* pp. 73, Joint Research Centre, European Commission, Ispra, Italy.

Bocchini, G.M., Novikova, T., Papadopoulos, G.A., Agalos, A., Mouzakiotis, E., Karastathis, V. & Voulgaris, N., 2020. Tsunami potential of moderate earthquakes: the July 1, 2009 earthquake (M_w 6.45) and its associated local tsunami in the Hellenic arc, *Pure appl. Geophys.,* **177**(3), 1315–1333.

Borrero, J.C., Lynett, P.J. & Kalligeris, N., 2015. Tsunami currents in ports, *Philos. T. R. Soc. A.,* **373**(2053), 20140372 , doi:10.1098/rsta.2014.0372.

Bouguet, J.-V., 2008. *Camera Calibration Toolbox for Matlab (2008),* Available at: http://www.vision.caltech.edu/bouguetj/calib_doc/index.html.

Briggs, M.J., Synolakis, C.E., Harkins, G.S. & Green, D.R., 1995. Laboratory experiments of tsunami runup on a circular island, in *Tsunamis: 1992–1994: Their Generation, Dynamics, and Hazard,* pp. 569–593, eds Imamura, F. & Satake, K., Birkhäuser Basel , doi:10.1007/978-3-0348-7279-9_12.

Burwell, D., Tolkova, E. & Chawla, A., 2007. Diffusion and dispersion characterization of a numerical tsunami model, *Ocean Model.,* **19**(1–2), 10–30.

Canitez, N., S.B. & Üçer, S.B., 1967. Computer determinations for the fault-plane solutions in and near Anatolia, *Tectonophysics,* **4,** 235–244.

Constantinescu, L., Ruprechtova, L. & Enescu, D., 1966. Mediterranean–Alpine earthquake mechanisms and their seismotectonic implications, *Geophys. J. Int.,* **10**(4), 347–368.

Derakhti, M., Dalrymple, R.A., Okal, E.A. & Synolakis, C.E., 2019. Temporal and topographic source effects on tsunami generation, *J. geophys. Res. Oceans,* **124**(7), 5270–5288.

Dogan, G.G. *et al.*, 2019. The 20th July 2017 Bodrum–Kos Tsunami field survey, *Pure appl. Geophys.,* **176**(7), 2925–2949.

Ebeling, C.W., Okal, E.A., Kalligeris, N. & Synolakis, C.E., 2012. Modern seismological reassessment and tsunami simulation of historical Hellenic Arc earthquakes, *Tectonophysics,* **530,** 225–239.

Engdahl, E.R. & Villaseñor, A., 2002. *Global seismicity, 1900–1999, in International Handbook of Earthquake and Engineering Seismology, Part A,* pp. 665–690, eds Lee, W.H.K., Kanamori, H. & Jennings, P., Academic Press, doi:10.1016/S0074-6142(02)80244-3.

England, P., Howell, A., Jackson, J. & Synolakis, C., 2015. Palaeotsunamis and tsunami hazards in the Eastern Mediterranean, *Philos. T. R. Soc. A.,* **373**(2053), 20140374 , doi:10.1098/rsta.2014.0374.

Fritz, H.M., Borrero, J.C., Synolakis, C.E. & Yoo, J., 2006. 2004 Indian Ocean tsunami flow velocity measurements from survivor videos, *Geophys. Res. Lett.,* **33**(24) , doi:10.1029/2006GL026784.

Flouri, E.T., Kalligeris, N., Alexandrakis, G., Kampanis, N.A. & Synolakis, C.E., 2013. Application of a finite difference computational model to the simulation of earthquake generated tsunamis, *Appl. Numer. Math.,* **67,** 111–125.

Fritz, H.M. *et al.*, 2012. The 2011 Japan tsunami current velocity measurements from survivor videos at Kesennuma Bay using LiDAR, *Geophys. Res. Lett.,* **39**(7) , doi:10.1029/2011GL050686.

GEONICA, 2015. *DATAMAR 2000C/3000C Micorwave (26 GHz) Radar Tide Gauge User's Manual Rev. 8,* Geonica S.A., Madrid, Spain.

Goodstein, J.R., Kanamori, H. & Lee, W.H.K., 1980. Seismology microfiche publications from the Caltech archives, *Bull. seism. Soc. Am.,* **70,** 657–658.

Gutenberg, B. & Richter, C.F., 1954. *Seismicity of the Earth and Associated Phenomena,* pp. 310, Princeton University Press.

Heidarzadeh, M., Necmioglu, O., Ishibe, T. & Yalciner, A.C., 2017. Bodrum–Kos (Turkey–Greece) M_w 6.6 earthquake and tsunami of 20 July 2017: a test for the Mediterranean tsunami warning system, *Geosci. Lett.,* **4**(1), 31 , doi:10.1186/s40562-017-0097-0.

Hellenic Mapping and Cadastral Organization (HEMCO), 1987. *The Hellenic Geodetic Reference System 1987. Report, Ministry of Environment, Urban Planning and Public Works (in Greek).*

Holland, K.T., Holman, R.A., Lippmann, T.C., Stanley, J. & Plant, N., 1997. Practical use of video imagery in nearshore oceanographic field studies, *IEEE J. Oceanic Eng.,* **22**(1), 81–92.

Jackson, J. & McKenzie, D., 1988. The relationship between plate motions and seismic moment tensors, and the rates of active deformation in the Mediterranean and Middle East, *Geophys. J.,* **93,** 45–73.

Jobert, N. & Jobert, G., 1983. An application of ray theory to the propagation of waves along a laterally heterogeneous spherical surface, *Geophys. Res. Lett.,* **10**(12), 1148–1151.

Kagan, Y.Y., 1991. 3-D rotation of double–couple earthquake sources, *Geophys. J. Int.,* **106,** 709–716.

Kalligeris, N., Skanavis, V., Tavakkol, S., Ayca, A., El Safty, H., Lynett, P. & Synolakis, C., 2016. Lagrangian flow measurements and observations of the 2015 Chilean tsunami in Ventura, CA, *Geophys. Res. Lett.,* **43**(10), 5217–5224.

Kânoğlu, U. & Synolakis, C.E., 1998. Long wave runup on piecewise linear topographies, *J. Fluid Mech.,* **374,** 1–28.

Kânoğlu, U., Titov, V., Bernard, E. & Synolakis, C., 2015. Tsunamis: bridging science, engineering and society, *Philos. T. R. Soc. A.,* **373**(2053), 20140369 , doi:10.1098/rsta.2014.0369.

Kim, D.-H., Lynett, P.J. & Socolofsky, S.A., 2009. A depth-integrated model for weakly dispersive, turbulent, and rotational fluid flows, *Ocean Model.,* **27**(3–4), 198–214.

Kiratzi, A.A. & Langston, C.A., 1989. Estimation of earthquake source parameters of the May 4, 1972 event of the Hellenic arc by the inversion of waveform data, *Phys. Earth planet. Inter.,* **57,** 225–232.

Le Pichon, X., Liberis, N., Angelier, J. & Renard, V., 1982. Strain distribution over the East Mediterranean Ridge: a synthesis incorporating new Sea-Beam data, *Tectonophysics,* **86,** 243–274.

Liu, P.L.F., Cho, Y.S., Briggs, M.J., Kânoğlu, U. & Synolakis, C.E., 1995. Runup of solitary waves on a circular island, *J. Fluid Mech.,* **302,** 259–285.

Lynett, P.J., Liu, P.-L.F., Sitanggang, K.I. & Kim, D.-H., 2002. *Modeling Wave Generation, Evolution, and Interaction with Depth-integrated, Dispersive Wave Equations COULWAVE Code Manual,* Cornell University Long and Intermediate Wave Modeling Package.

Lynett, P.J., Borrero, J.C., Son, S., Wilson, R. & Miller, K., 2014. Assessment of the tsunami–induced current hazard, *Geophys. Res. Lett.,* **41,** 2048–2055.

Maravelakis, N., Kalligeris, N., Lynett, P.J., Skanavis, V. & Synolakis, C.E., 2021. Wave overtopping due to harbour resonance, *Coast. Eng.,* **169,** 103973 , doi:10.1016/j.coastaleng.2021.103973.

Marcos, M., Liu, P.L.F. & Monserrat, S., 2004. Nonlinear resonant coupling between two adjacent bays, *J. geophys. Res. Oceans,* **109**(C5) , doi:10.1029/2003JC002039.

Newman, A.V. & Okal, E.A., 1998. Teleseismic estimates of radiated seismic energy: the E/M0 discriminant for tsunami earthquakes, *J. geophys. Res.,* **103,** 26885–26898.

Niu, X., 2021. Resonance of long waves around a circular island and its relation to edge waves, *Eur. J. Mech.,* **86,** 15–24.

Nocquet, J.-M., 2012. Present-day kinematics of the Mediterranean: A comprehensive overview of GPS results, *Tectonophysics,* **579,** 220–242.

Nwogu, O., 1993. Alternative form of Boussinesq equations for nearshore wave propagation, *J. Waterw. Port C-ASCE,* **119**(6), 618–638.

Okada, Y., 1985. Surface deformation due to shear and tensile faults in a half-space, *Bull. seism. Soc. Am.,* **75**(4), 1135–1154.

Okal, E.A. & Talandier, J., 1989. M_m: a variable period mantle magnitude, *J. geophys. Res.,* **94,** 4169–4193.

Okal, E.A. & Talandier, J., 1990. M_m: extension to Love waves of the concept of a variable–period mantle magnitude, *Pure appl. Geophys.,* **134,** 355–384.

Okal, E.A. & Synolakis, C.E., 2008. Far-field tsunami hazard from mega-thrust earthquakes in the Indian Ocean, *Geophys. J. Int.,* **172,** 995–1015.

Okal, E.A., 2013. From 3–Hz P waves to ${}_0S_2$: no evidence of a slow component to the source of the 2011 Tohoku earthquake, *Pure appl. Geophys.,* **170,** 963–973.

Okal, E.A., 2015. The quest for wisdom: lessons from 17 tsunamis, 2004–2014, *Philos. T. R. Soc. A.,* **373**(2053), 20140370 , doi:10.1098/rsta.2014.0370.

Okal, E.A. & Saloor, N., 2017. Historical tsunami earthquakes in the Southwest Pacific: an extension to $\Delta > 80°$ of the energy-to-moment parameter Θ, *Geophys. J. Int.,* **210,** 852–873.

Pix4D, S.A., 2017. *Pix4Dmapper 4.1 User Manual,* Pix4D SA, Lausanne, Switzerland.

Rabinovich, A.B., 1997. Spectral analysis of tsunami waves: Separation of source and topography effects, *J. geophys. Res. Oceans,* **102**(C6), 12663–12676.

Rabinovich, A.B., 2009. Seiches and harbor oscillations, in *Handbook of Coastal and Ocean Engineering,* pp. 193–236, ed. Kim, Y.C., World Scientific, Singapore , doi:10.1142/9789812819307_0009.

Rees, B.A. & Okal, E.A., 1987. The depth of the deepest historical earthquakes, *Pure appl. Geophys.,* **125,** 699–715.

Ritsema, A.R., 1974. The earthquake mechanisms of the Balkan region, *Kon. Ned. Meteor. Inst. Repts,* **74**(4), 34.

Ryan, W.B.F., Stanley, D.J., Hersey, J.B., Fahlquist, D.A. & Allan, T.D., 1970. The tectonics and geology of the Mediterranean Sea, in *The Sea,* Vol. **4(II),** pp. 387–492, Wiley Interscience, New York.

Satake, K., 1988. Effects of bathymetry on tsunami propagation: application of ray tracing to tsunamis, *Pure appl. Geophys.,* **126**(1), 27–36.

Storchak, D.A., Di Giacomo, D., Engdahl, E.R., Harris, J., Bondár, I., Lee, W.H.K., Bormann, P. & Villaseñor, A., 2019. The ISC–GEM global instrumental earthquake catalogue (1900–2009): introduction, *Phys. Earth planet. Inter.,* **239,** 48–63.

Synolakis, C.E. & Okal, E.A., 2005. 1992–2002: perspective on a decade of post-tsunami surveys, in *Tsunamis: Case Studies and Recent Developments,* pp. 1–29, ed. Satake, K., Springer, Dordrecht , doi:10.1007/1-4020-3331-1_1.

Synolakis, C.E., Kalligeris, N., Flouri, E., Alexandrakis, G. & Kampanis, N., 2008a. The great cretan splash up-a coastal disaster preparedness exercise in Greece, in *Solutions to Coastal Disasters 2011,* pp. 396–407.

Synolakis, C.E., Kalligeris, N., Foteinis, S. & Voukouvalas, E., 2008b. The plight of the beaches of Crete, in *Solutions to Coastal Disasters 2008,* 495–506.

Ta Nea, 2009. *Newspaper Article (in Greek) with Title: Mini Tsunami south of Crete from 5.9 Earthquake* , Available at: https://www.tanea.gr/2009/07/02/greece/mini-tsoynami-notia-tis-kritis-apo-ta-5-9-rixter/ Last accessed on 2021 June 13.

Taymaz, T., Jackson, J.A. & Westaway, R., 1990. Earthquake mechanisms in the Hellenic Trench near Crete, *Geophys. J. Int.,* **102,** 695–731.

Taymaz, T., Jackson, J. & McKenzie, D., 1991. Active tectonics of the north and central Aegean Sea, *Geophys. J. Int.,* **106**(2), 433–490.

Titov, V.V. & Synolakis, C.E., 1995. Modeling of breaking and nonbreaking long-wave evolution and runup using VTCS-2, *J. Waterw. Port C-ASCE,* **121**(6), 308–316.

Titov, V.V. & Synolakis, C.E., 1998. Numerical modeling of tidal wave runup, *J. Waterw. Port C-ASCE,* **124**(4), 157–171.

Titov, V.V., Kânoğlu, U. & Synolakis, C.E., 2016. Development of MOST for real-time tsunami forecasting, *J. Waterw. Port C—ASCE,* **142**(6), 03116004 , doi:10.1061/(ASCE)WW.1943-5460.0000357.

Torrence, C. & Compo, G.P., 1998. A practical guide to wavelet analysis, *B. Am. Meteorol. Soc.,* **79**(1), 61–78.

Valle, B.L., Kalligeris, N., Findikakis, A.N., Okal, E.A., Melilla, L. & Synolakis, C.E., 2014. Plausible megathrust tsunamis in the eastern Mediterranean Sea, *Proc. Inst. Civ. Eng.: Eng. Comput. Mech.,* **167**(3), 99–105.

Veis, G., 1996. *National report of Greece. Report on the Symp. of the IAG Subcommission for the European Reference Frame (EUREF), Ankara, 22–25 May 1996. Report,* Verlag der Bayerischen Akademie der Wissenschaften, Heft Nr. 57.

Vela, J., Pérez, B., González, M., Otero, L., Olabarrieta, M., Canals, M. & Casamor, J.L., 2011. Tsunami resonance in the Palma de Majorca bay and harbor induced bythe 2003 Boumerdes-Zemmouri Algerian earthquake (Western Mediterranean), *Coastal Eng. Proc.,* **1**(32) , doi:10.9753/icce.v32.currents.7.

Welch, P., 1967. The use of fast Fourier transform for the estimation of power spectra: a method based on time averaging over short, modified periodograms, *IEEE Trans. Audio Electroacoust.,* **15**(2), 70–73.

Wells, D.L. & Coppersmith, K.J., 1994. New empirical relationships among magnitude, rupture length, rupture width, rupture area, and surface displacement, *Bull. seism. Soc. Am.,* **84**(4), 974–1002.

Woods, M.T. & Okal, E.A., 1987. Effect of variable bathymetry on the amplitude of teleseismic tsunamis: a ray-tracing experiment, *Geophys. Res. Lett.,* **14**(7), 765–768.

Winterl, A., Richter, S., Houstin, A., Nesterova, A.P., Bonadonna, F., Schneider, W., Fabry, B., Le Bohec, C. & Zitterbart, D.P., 2020. micrObs—a customizable time-lapse camera for ecological studies, *HardwareX.,* **8,** e00134 , doi:10.1016/j.ohx.2020.e00134.

Wysession, M.E., Okal, E.A. & Miller, K.L., 1991. Intraplate seismicity of the Pacific Basin, 1913–1988, *Pure appl. Geophys.,* **135,** 261–359.

Yeh, H., Imamura, F., Synolakis, C., Tsuji, Y., Liu, P. & Shi, S., 1993. The Flores island tsunamis, *Eos, Trans. Am. geophys. Un.,* **74**(33), 369–373.

APPENDIX A: TSUNAMI WARNING

The TSPs that are monitoring the Eastern Mediterranean within the Intergovernmental Coordination Group of the North East Atlantic, Mediterranean and Connected seas Tsunami Warning System of UNESCO (ICG/ NEAMTWS) are NOA-HLNTWC (National Observatory

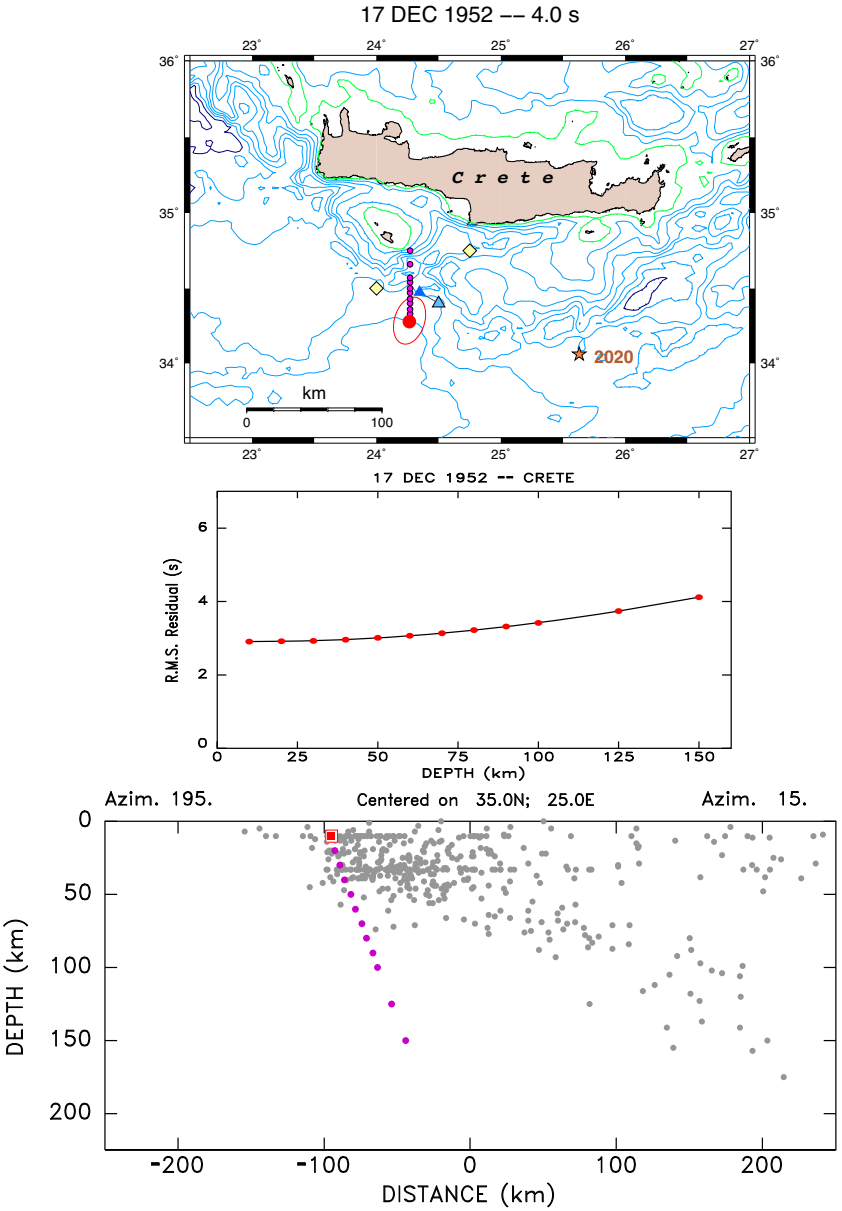

Figure A1. Relocation of the 1952 earthquake. All symbols are defined in Appendix B.

of Athens—Hellenic National Tsunami Warning Centre in Greece), CAT-INGV (Centro Allerta Tsunami—Istituto Nazionale di Geofisica e Vulcanologia in Italy) and KOERI-RETMC (Kandilli Observatory and Earthquake Research Institute—Regional Earthquake and Tsunami Monitoring Center in Turkey). The alert level of the initial message was regional advisory for NOA-HLNTWC, local watch for CAT-INGV and regional advisory for KOERI-RETMC. In the ongoing messages sent by NOA-HLNTWC and KOERI-RETMC, the alert level was elevated to regional watch.

APPENDIX B: HISTORICAL EVENTS

We detail here the case of the four major historical events shown as grey triangles on the top frame of Fig. 1, proceeding backwards in time.

In all cases, we relocate the earthquake based on arrival times listed by the International Seismological Center, and if not available, on B. Gutenberg's personal notepads (Goodstein *et al.* 1980). We use the interactive, iterative method of Wysession *et al.* (1991) which derives an ellipse of confidence from a Monte Carlo algorithm injecting Gaussian noise into the data set. The standard deviation of that noise increases backwards with time, from 1 s for a modern earthquake (past-1962) to 10 s in the 1910s and 15 s in 1900. In most cases, the inversion cannot resolve the hypocentral depth, which has to be kept constant, but we then study the evolution of the rms residual of the relocation, as well as the moveout of the epicentre, as a function of the fixed value of depth. This procedure can provide constraints on hypocentral depth (Rees & Okal 1987).

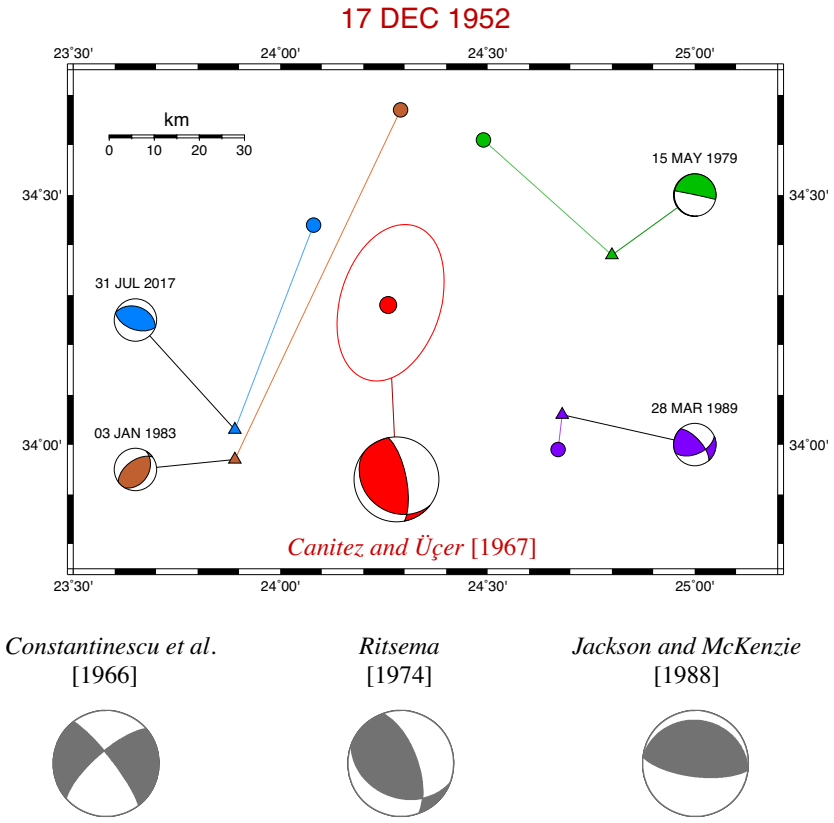

Figure A2. Focal mechanisms of the 1952 earthquake and neighbouring events. The map reproduces our relocation, with associated ellipse, and the preferred mechanism of Canitez & Üçer (1967). The focal mechanisms of the four closest GlobalCMT solutions are also shown; note the large disparity in geometries. For each event, the colour-coded solid dot represents the relocated ISC epicentre, and the triangle the GCMT centroid; note the occasional large distance between them. Alternate focal solutions for the 1952 are also shown in grey below the map.

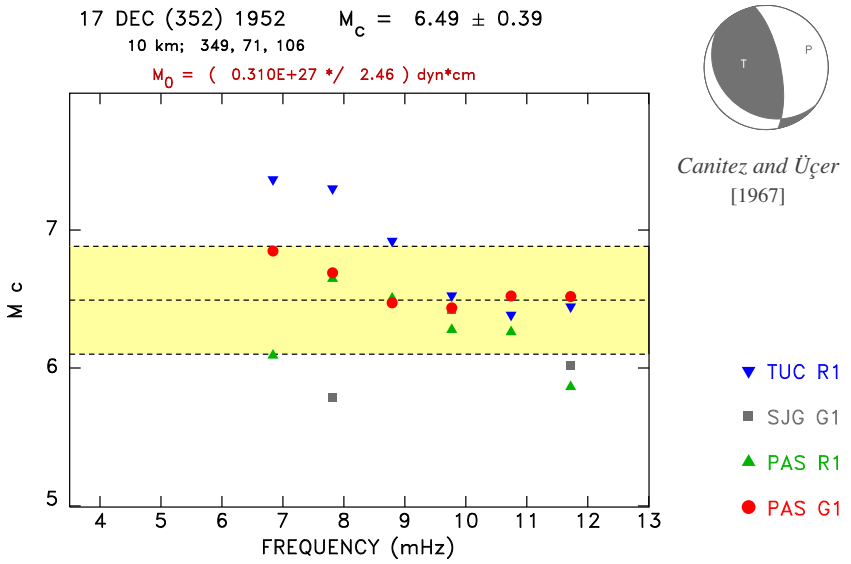

Figure A3. Mantle magnitudes computed as a function of frequency for the 1952 event, in Canitez & Üçer (1967) focal geometry, using Rayleigh waves at Pasadena and Tucson, and Love waves at Pasadena and San Juan. The yellow band is a 1–σ confidence interval about the average value corresponding to a moment of 3×10^{19} N·m.

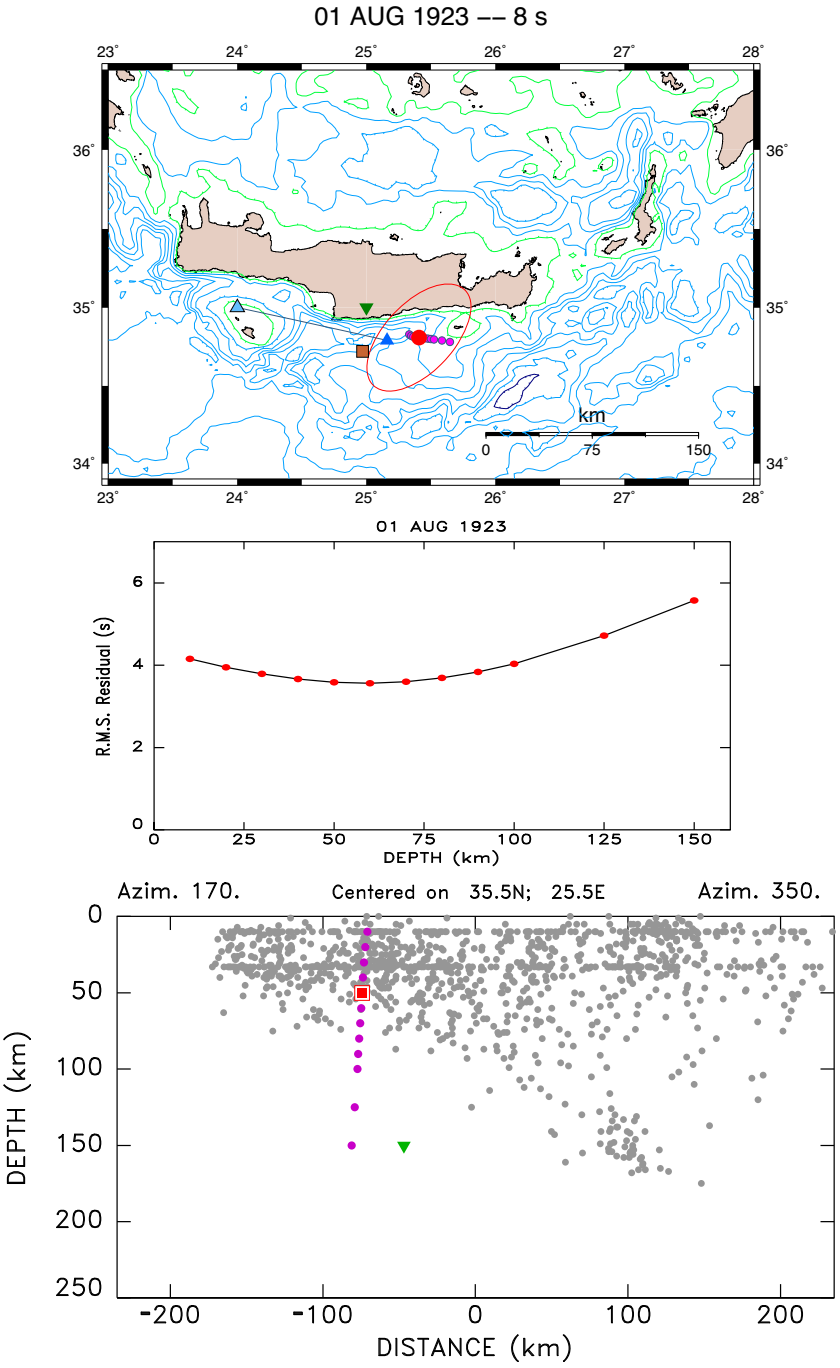

Figure A4. Relocation of the 1923 earthquake. All symbols are defined in Appendix B.

In all the figures of this appendix, on the top frame for each event, the light blue triangle is the epicentre of the original location from the International Seismological Summary [ISS], the dark blue triangle the recent relocation by the ISC under the ISC–GEM program (Storchak *et al.* 2019), the inverted green triangle (Gutenberg & Richter 1954) location, and the brown square the Centennial catalogue's (Engdahl & Villaseñor 2002) epicentre when independently relocated. The red dot and associated ellipse are the results of our relocation. The small purple dots illustrate the moveout of the epicentre upon an increase in depth from 10 to 150 km. The variation of residuals with constrained depth is shown on the centre frame, and the bottom frame shows a cross-section of the 3-D moveout of the solution against the background of recent seismicity, defined as NEIC solutions postdating 1970 and with at least one magnitude ≥4.5.

B1 1952 December 17; $M_{PAS} = 6.8$

This is the largest historical earthquake recorded in the area. To our knowledge, there are no tsunami reports for this event, which however took place at night during very stormy weather, thus minimizing human perception. Fig. A1 displays available epicentral estimates as well

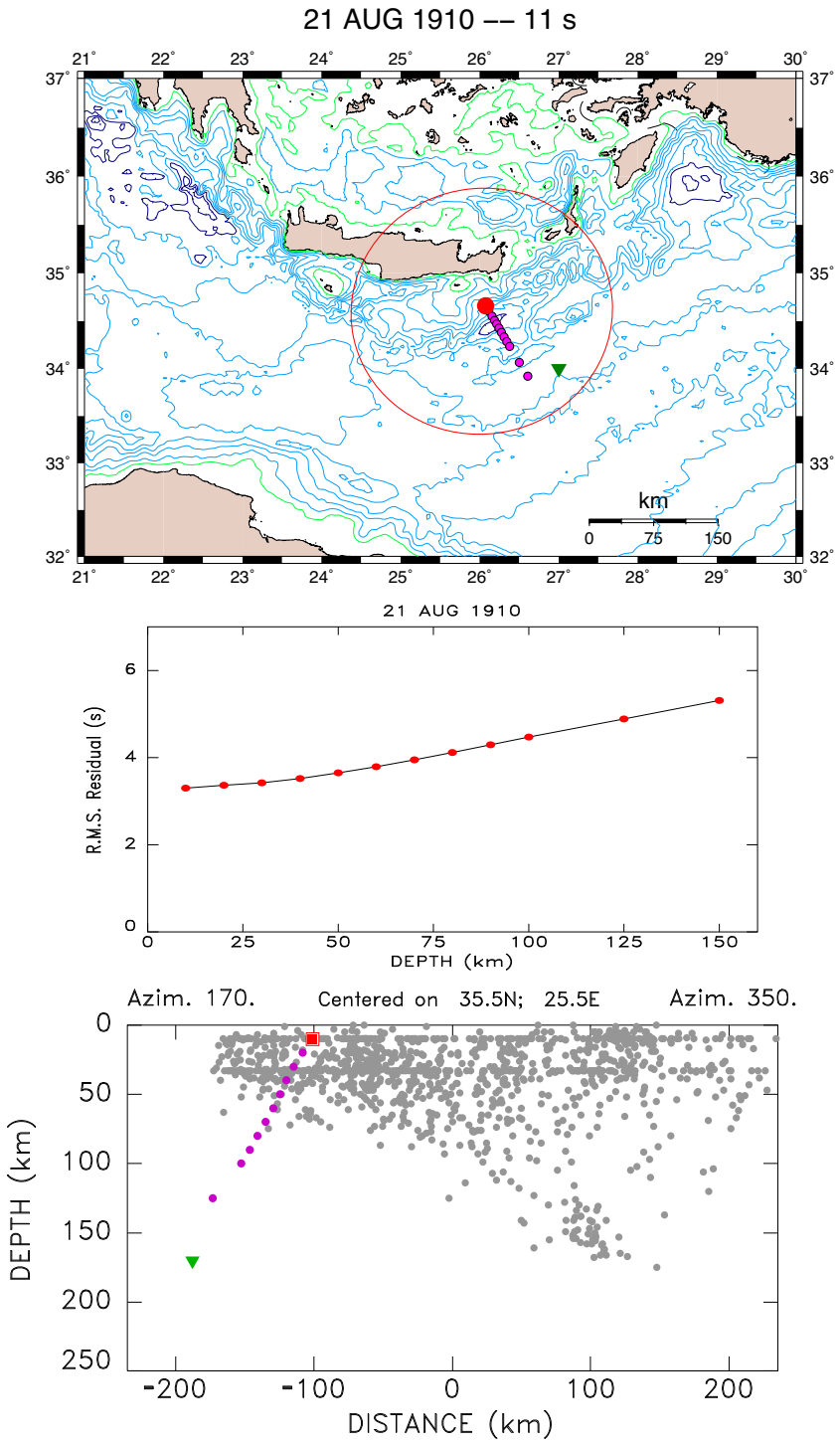

Figure A5. Relocation of the 1910 earthquake. All symbols are defined in Appendix B.

as the result of our relocation based on 196 arrival times listed in the ISS, with its Monte Carlo ellipse ($\sigma_G = 4$ s). The event is not listed in Gutenberg & Richter (1954) *Seismicity of the Earth*, presumably because it is too close to its publication date, and was not relocated as part

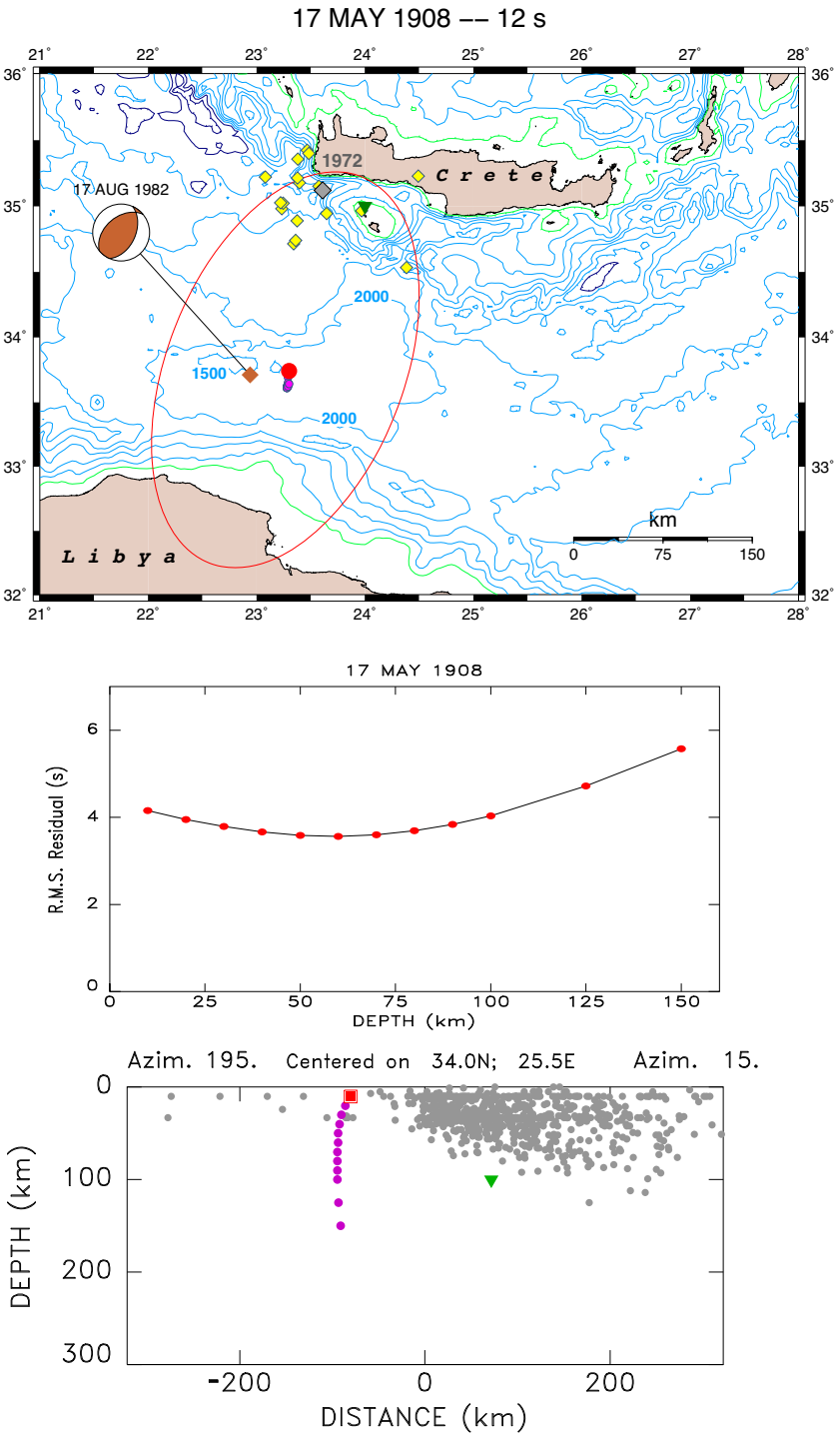

Figure A6. Relocation of the 1908 earthquake. The East Mediterranean Ridge is identified by the local 2000 and 1500-m contours. The brown diamond and associated beachball show the 1982 earthquake (Taymaz *et al.* 1990). On the top frame, the yellow diamonds show modern background seismicity ($50 \leq h \leq 75$ km; $m_b \geq 4.5$) at the apex of our confidence ellipse. The grey diamond locates the 1972 mantle event (Kiratzi & Langston 1989).

of the Centennial catalogue. Rms residuals increase monotonically (if slowly) with depth and the cross-section in Fig. A1 clearly rules out any depth greater than 65 km.

Several focal mechanisms were published for the 1952 event. Constantinescu *et al.* (1966) proposed a strike–slip mechanism which offers only a poor fit to the polarities reported to the ISC. Jackson & McKenzie (1988) proposed pure shallow-angle thrusting on a North-dipping plane, while Canitez & Üçer (1967) and Ritsema (1974) published more oblique mechanisms (see Fig. A2).

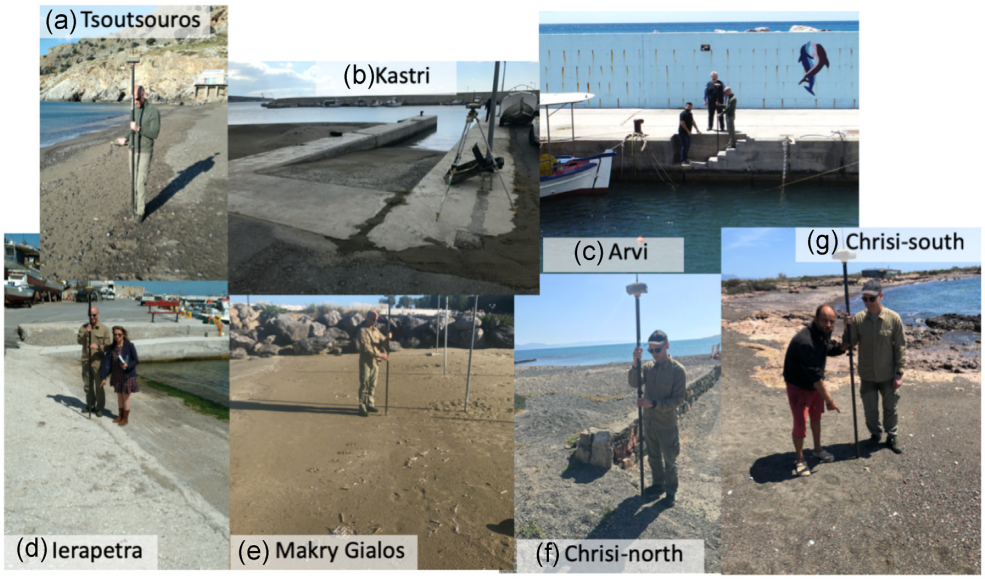

Figure A7. Pictures of tsunami runup data collected in seven coastal locations.

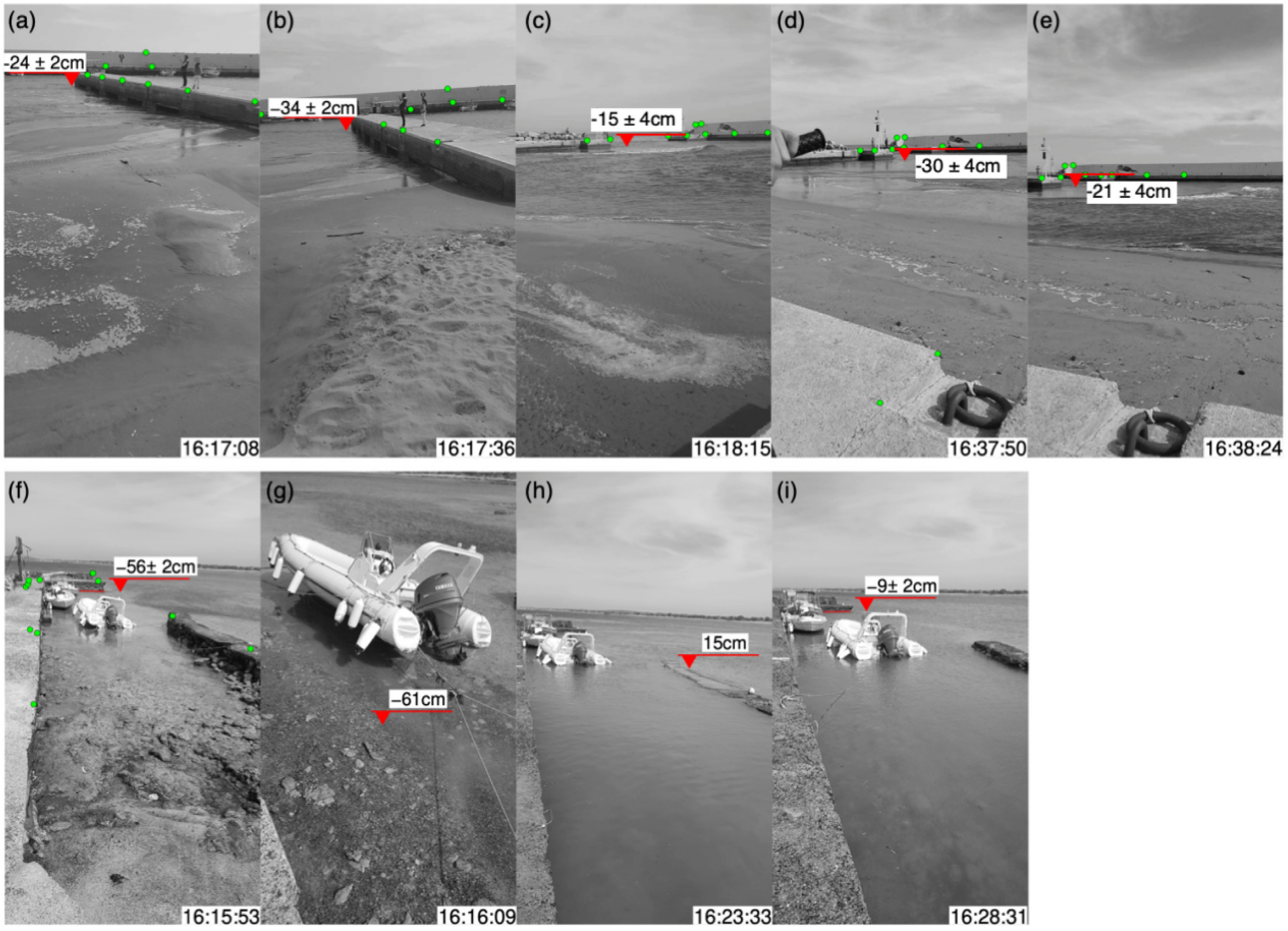

Figure A8. Still images of the tsunami provided by eyewitnesses in the harbours in Arvi (top row) and north Chrisi (bottom row). The precise timestamps (in local time) of the original pictures are shown on the bottom right. The images in Arvi are frames of 1080 × 1920 resolution extracted from two separate videos; all water levels were extracted through image analysis. The 2268 × 4032 resolution images in Chrisi were captured on a cellphone; the water level of the first and fourth pictures was extracted using image analysis, and the water elevation of the second and third through *in situ* topographic measurements. The GCP's used for the camera extrinsic parametrization are shown with the green circles.

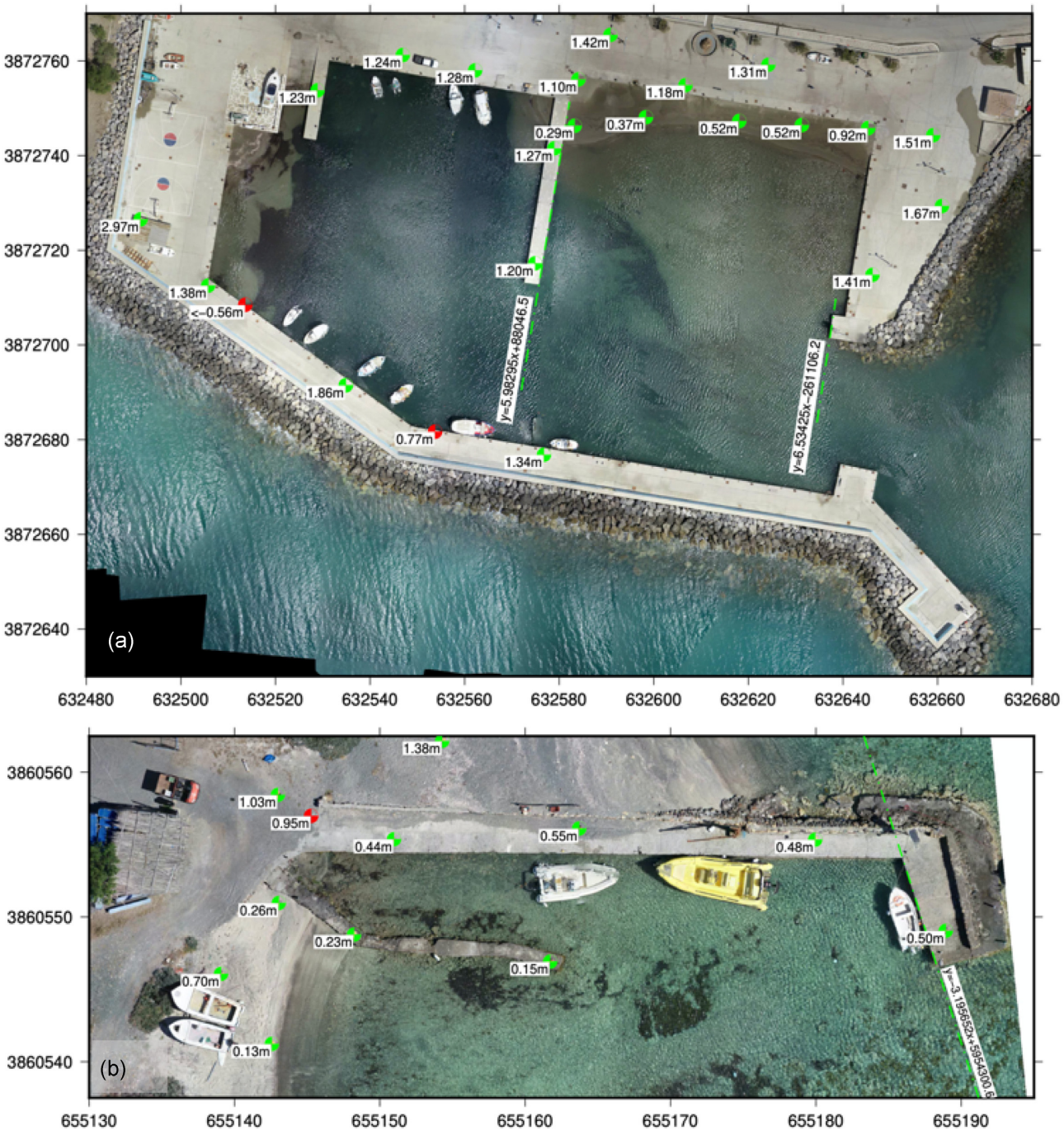

Figure A9. Orthophoto maps of the harbours in (a) Arvi and (b) north Chrisi, produced using drone aerial images. The GCP's used for the orthorectification and the corresponding elevations are shown with the green points. The surveyed runup/drawdown points are shown in red. The lines projected along docks that were used to extract the water level from eyewitness images (Fig. A8) are shown with the green dashed–dotted lines. Grid coordinates correspond to the (projected) Hellenic Geodetic Reference System 1987 (HEMCO 1987; Veis 1996): *x*-axis corresponds to the Easting (m) and the *y*-axis to the Northing (m).

We estimated a seismic moment from surface waves obtained at Tucson, Pasadena and San Juan, using the mantle magnitude formalism of Okal & Talandier (1989, 1990). The scatter in moment values is minimized in Canitez & Üçer (1967) focal geometry (Fig. A3), which yields an average moment of 3×10^{19} N·m ($M_w = 6.9$), in good agreement with the value of $M_{PAS} = 6.8$ assigned by B. Gutenberg (Goodstein *et al.* 1980). Note on Fig. A3 the large scatter in mechanisms among the 1952 event and its closest neighbours in the GlobalCMT catalogue.

B2 1923 August 01; $M_{PAS} = 6.7$

The earthquake was initially located by the ISS South of Western Crete, at 35°N, 24°E (with no indication of depth), and moved East to 35°N, 25°E at a depth of 150 km by Gutenberg & Richter (1954). The Centennial project moved it about 30 km South at a (fixed) depth of 35 km,

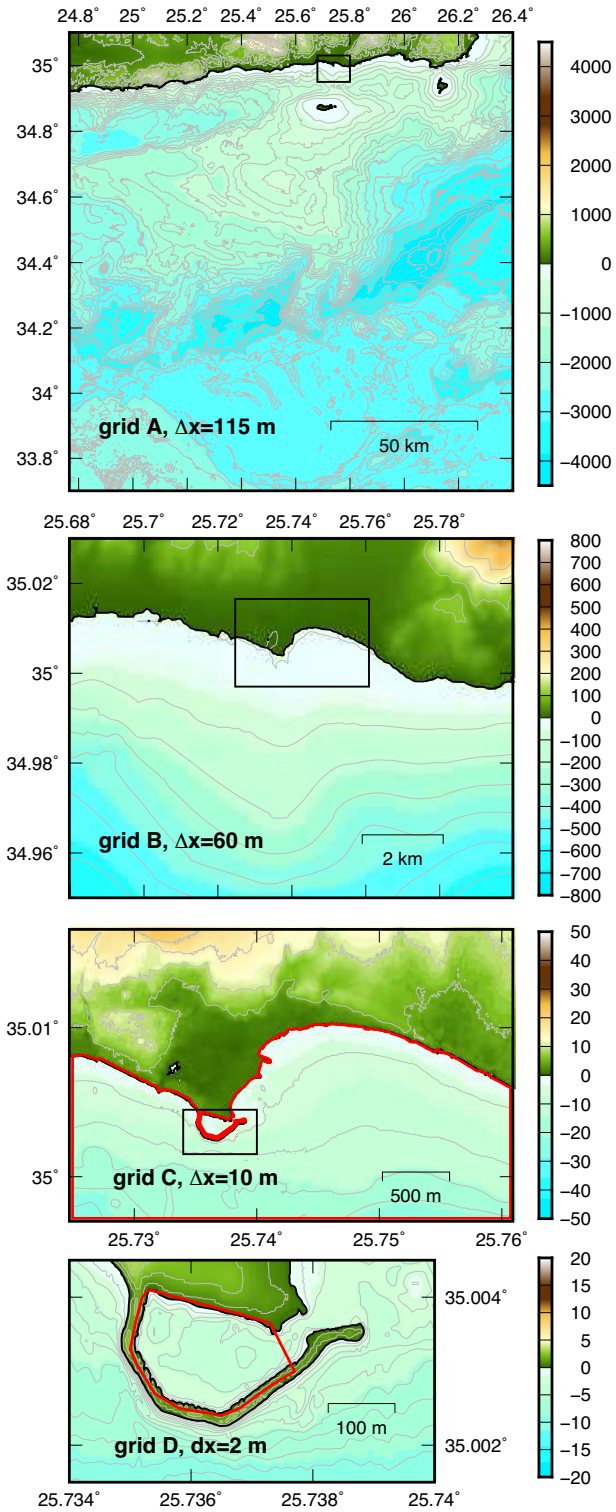

Figure A10. Numerical relief grids used for hydrodynamic modelling. Contours for grids A, B, C and D drawn every 200, 100, 5 and 1 m, respectively. Colour bars show relief values in metres. Red polygons plotted on grids C and D denote the regions over which the free surface elevation time-series were averaged, as described in Section 5.3.

while the modern ISC–GEM locates it slightly East at 34.79°N, 25.16°E, using a constrained depth of 15 km. We relocate it at 34.81°N; 25.41°E (Fig. A4).

The rms of residuals is minimized at around 60 km depth, with the moveout of the epicentres oriented Eastwards, outside the trend of the Wadati–Benioff Zone. It is clearly impossible to reconcile modern relocations with the depth proposed by Gutenberg & Richter (1954). We prefer a depth of around 50 km, inside a 3-D zone with sustained background seismicity, albeit at lower magnitudes.

Table A1. Tsunami field data measurements for the 2020 tsunami in south Crete.

Site	Lat (°N)	Lon (°E)	Runup RU (m)	Drawdown DD (m)	Description
Tsoutsouros west beach	34.98371	25.28067	0.56	–	Wrack line, not confirmed by eyewitness.
Tsoutsouros harbour	34.98473	25.28615	>0.24	–	Measured on slipway, indicated by eyewitness.
Tsoutsouros harbour	34.98469	25.28615	–	<−0.40	Measured on slipway, indicated by eyewitness.
Kastri harbour	34.99802	25.37168	0.87	–	Sand deposit on top of slipway, confirmed by eyewitness.
Kastri harbour	34.99751	25.37255	–	<-0.97	Distance between boat's rudder and seafloor, indicated by eyewitness.
Arvi harbour	34.99064	25.45403	0.77	–	Measured on harbour dock stairs as indicated by eyewitness.
Arvi harbour	34.99088	25.45359	–	<−0.56	Underwater dock pipeline exposed during drawdown, indicated by eyewitness.
Ierapetra harbour	35.00407	25.73537	0.32	–	Measured on slipway as indicated by eyewitness - confirmed from picture.
Makry Gialos beach	35.03771	25.97359	0.35	–	Wrack line, confirmed by eyewitness.
Chrisi north harbour	34.87814	25.69922	0.95	–	Measured on dock as indicated by eyewitness - confirmed from picture.
Chrisi north habour	34.87809	25.69944	–	−0.86	Maximum drawdown, indicated by eyewitness.
Chrisi south beach	34.86898	25.71270	0.61	–	Wrack line, confirmed by eyewitness.

Table A2. Drone flight altitude and parameters of the resulting point clouds.

Site	Flight altitude (m)	Point cloud resolution (cm)	Error (cm)	Error/ pixel (−)
Arvi, entire harbour	70	1.28	2.2	0.271
Arvi, inner harbour	30	0.78	1.5	0.288
Chrisi	45	0.58	1.6	0.346

Table A3. Spatial resolution of numerical grids used for the hydrodynamic simulations.

Grid name	Model codename	Data source	Grid cell size (arc min)	Grid cell size (m)
A	MOST-3G-4G	EMODNet (2018)	1/16	–
B	MOST-3G-4G	EMODNet (2018)	0.03	–
C	MOST-3G-4G	HHS, 2 and 10 m DTMs	0.0054	–
D	MOST-4G	HHS, 2 m DTM	0.0011	–
A-COUL	COUL	EMODNet (2018), HHS, DTMs	–	30

B3 1910 August 21; $M_{PAS} = 6.5$

This is another case of intermediate depth (this time 170 km) proposed by Gutenberg & Richter (1954); their solution is all the more intriguing since it is displaced significantly South of the trench. No solutions are available from the ISS or the ISC. Based on 13 *P* and *S* times listed on B. Gutenberg's notepads (Goodstein *et al.* 1980), we relocate the earthquake to the North at 34.66°N, 26.07°E (Fig. A5). The residuals show a regular, monotonic increase with depth, and the epicentre moveout with depth is actually Southeastwards, against the trend of the Wadati–Benioff Zone. All this evidence argues for a very shallow depth.

B4 1908 May 17; $M_{PAS} = 6.8$

Once again, Gutenberg & Richter (1954) list this earthquake at an intermediate depth of 100 km, with an epicentre at 35°N, 24°E. Their solution is copied verbatim into the Centennial catalogue, and there are no ISS or ISC solutions. Based on 16 arrival times listed on B. Gutenberg's notepads (Goodstein *et al.* 1980), we obtain a solution considerably displaced, about 200 km SSW, to 33.74°N, 23.30°E (Fig. A6). It is remarkable that this locates on the East Mediterranean Ridge, a feature interpreted by Ryan *et al.* (1970) and Le Pichon *et al.* (1982) as an accretionary structure unable to subduct and squeezed in the closing straits between Libya and Crete. As shown on Fig. A6, a modern thrust faulting earthquake ($M_0 = 4 \times 10^{18}$ N·m) took place only 37 km to the West on 1982 August 17 (Taymaz *et al.* 1990). Additional seismicity is also documented at lower magnitudes in the area.

Our relocation cannot resolve depth, and while a minimum rms residual is found around 50 km, all depths down to 100 km yield residuals differing by no more than 1 s. The inverted epicentre is remarkably robust, with moveout of no more than 20 km. The 1982 earthquake is listed with a centroid depth of 23 km in the GlobalCMT catalog, but Taymaz *et al.* (1990) detailed body-wave modelling places it at 35 km, which

would locate it in the mantle. Under this scenario, the most plausible interpretation of the 1908 earthquake would be to make it an earlier equivalent to the 1982 event. Given their grossly comparable magnitudes, one could offer a speculative estimate on the order of 5 mm yr^{-1} for the rate of WNW–ESE shortening in the area, which is a fraction of the 35 mm yr^{-1} ENE–WSW convergence estimated by Nocquet (2012) across the Cretan trench.

However, given the poor resolution of our relocation, with the Monte Carlo ellipse extending from Libya to Crete in a largely NS direction, we cannot totally rule out Gutenberg & Richter (1954) epicentre; their depth seems however excessive since modern GlobalCMT solutions at the northern apex of our confidence ellipse do not extend past 45 km, with smaller background seismicity listed down to 75 km. Under this model, the 1908 event could be similar to the thrust faulting earthquake of 1972 May 04 (Ritsema 1974; Kiratzi & Langston 1989; Taymaz *et al.* 1990).

B5 1918 July 16; $M_{PAS} = 6.5$

For reference, we mention this event, located by Gutenberg & Richter (1954) at 35.5°N, 25.5°E, that is, off the Northern coast of Crete, at a depth of 150 km, since it could *a priori* have happened South of the island, given the imprecision of their locations for older shocks. The earthquake relocates Northwest of Karpathos, at 35.96°N, 26.70°E, at a floated depth of 63 km, and its Monte Carlo ellipse does not reach the open sea South of Crete, and thus stays outside our study area. It could be similar to the earthquake of 1948 February 09 (Ebeling *et al.* 2012).

APPENDIX C: EQUIPMENT AND METHODS USED IN THE FIELD SURVEY

The tsunami post-reconnaissance team was equipped with an RTK GNSS system (Hiper Pro, Topcon) and a drone (DJI Phantom 4 Pro). The GNSS system was used in the field to collect data points related to the local tsunami effects, such as wave runup and drawdown. It was also used in combination with the drone to create high-resolution Digital Terrain Models (DTMs) in two locations (see Appendix E). The GNSS system consists of a base and a rover; the base station collects static GNSS data, while the surveyor collects field data with the rover. The measurements were post-processed using GNSS data from reference stations in Agios Nikolaos and Sitia, with baseline distances to Ierapetra of 20 and 40 km, respectively. The resulting mean error of the base station positions in the horizontal is 1 and 3 cm in the vertical. Due to the relatively large baseline distances, elevations in each location were referenced to the sea level.

APPENDIX D: DETAILED POST-TSUNAMI FIELD SURVEY FINDINGS

The main findings of the post-tsunami field survey are outlined in Section 3.1. This section provides the field survey data points in tabular form (Table A1) and a more detailed description of the findings in each coastal location visited.

D1 Ierapetra

Ierapetra is the most populous town on the south coast of Crete and the third most populous of Lasithi, the eastern regional unit of Crete. It has a harbour built in the Venetian era and later expanded by building a breakwater that protects it from southern and western storms. Today the harbour offers shelter for fishing and recreational boats. The tide gauge recording in Ierapetra offers the most detailed quantitative signature of the generated tsunami (Section 4). The maximum runup point inside the harbour of Ierapetra was determined through a picture showing the flood extent on the harbour slipway that was circulated in the media, while the precise location measured was confirmed by an eyewitness (Fig. A7d). In terms of the qualitative effects of the tsunami inside the harbour basin, we had the chance to interview three fishermen who were near or on their boats during the arrival of the tsunami, and all three claimed that the sea withdrew first and then advanced. While the coast guard closed the harbour after the tsunami warning was issued and all boats were docked, all three fishermen estimated that the tsunami-induced currents in the harbour were not strong enough to cause navigation problems.

D2 Tsoutsouros

Tsoutsouros is a coastal village ∼41 km west of Ierapetra and it is the last town before a 24 km stretch of rocky coastline, with the next settlement being the remote town of Ag. Ioannis further west. Tsoutsouros features two beaches, interrupted by a small fishing harbour. We first visited the sandy beach west of the harbour, where a distinct wrack line was visible at 56 cm above the water level at the time of the earthquake (Fig. A7a). We spoke to two local residents, but neither observed the tsunami on the beach, and thus they could not confirm that the wrack line formed as the result of tsunami runup on this beach. Two other residents whom we spoke to observed the tsunami in the harbour. Both were at home at the time of the earthquake. The first drove to the harbour approximately 10 min after the earthquake and captured the tsunami impacting the harbour entrance on video with his cellphone. He was filming while standing in front of a pebble beach just east of the harbour entrance, however he was not able to indicate where the tsunami had reached on the beach. While the inundation height was not confirmed with an *in situ* measurement, it appears to be consistent with the elevation of the wrack line observed on the beach west of the harbour. The other resident we interviewed drove to the harbour approximately 30 min after the earthquake, and he stood right next to the harbour's slipway while observing the tsunami inside the harbour. He was able to point to the minimum and maximum level the water reached while he was there, which were both measured with the GPS. Since the eyewitness was not present during the first three energetic tsunami waves, these measurements can only be considered as the minimum drawdown and runup in the harbour of Tsoutsouros.

D3 Kastri (Keratokampos)

Kastri/Keratokampos is a coastal village located 8 km east of Tsoutsouros that also features a small fishing harbour. We spoke to fishermen who were able to provide detailed tsunami observations in the harbour basin. One fisherman said that the water level dropped low enough for his docked boat to hit the seafloor; we measured the vertical distance from the rudder of the boat to the seafloor to be ∼1 m. The same fisherman pointed out where he remembers the maximum water level reaching along the south dock and this point measures at 59 cm vertical relative to the sea level at the time of the earthquake. On the north side of the harbour, a beach has formed just east of the slipway due to alongshore sediment transport being blocked by the harbour that was constructed right on the beach; harbour basin siltation is a widespread phenomenon in this area (Synolakis *et al.* 2008b). The fisherman also pointed out that the maximum water level reached the top of the slipway. This was confirmed from sand deposits found on a small depression at the top of the slipway (Fig. A7b). This runup point of 0.87 m elevation was the second highest measured in the field survey.

D4 Arvi

Arvi is another coastal village with a small fishing harbour about 8 km east of Kastri. Several eyewitness videos of the tsunami captured in the harbour of Arvi were shared in social media and we were able to interview six eyewitnesses during the survey; image analysis of two eyewitness videos captured in Arvi is described in Appendix E. The runup point for Arvi of 0.77 m was measured on a staircase along the southern dock (Fig. A7c), as indicated by an eyewitness. The same eyewitness described that a pipeline beneath the dock (designed for water recirculation in the basin) was exposed to the air during drawdown; this point was measured at 65 cm below sea level.

Most eyewitnesses in Kastri and Arvi observed the water level first dropping and most noted that the second wave was the largest. According to the eyewitnesses, the water level drop and rise were repeated at least six times with recurrence period between 6 and 7 min. More than half the eyewitnesses did not feel the earthquake and just one in five eyewitnesses moved to higher ground upon observing the strange behaviour of the sea. We found no evidence of the tsunami warning reaching these communities. It also worth noting that according to two eyewitnesses, a group of teenagers was swimming in a nearby beach during the earthquake. They did not feel the earthquake but they were warned by their parents to come out of the water in case tsunami waves would be generated. The overall conclusions from our visit in these two locations is that using their knowledge from prior tsunamis the locals expected the earthquake to generate tsunami waves but most decided to stay near the coast to observe the waves and currents without fleeing to higher ground.

D5 Sidonia and Gra Lygia

The reconnaissance team interviewed locals at Sidonia and Gra Lygia for tsunami sightings. In Sidonia, the locals described that the sea was agitated the day of the earthquake due to strong western winds and that nobody observed the tsunami on the beach. In Gra Lygia, located about 4 km west of Ierapetra, two groins/docks have been built off the beach for boats to dock during the summer. The team interviewed three residents living on the beachfront, but none of them observed the sea after the earthquake.

D6 Myrtos and Ferma

Myrtos and Ferma are two coastal villages with small craft shelters. The shelter in Myrtos was built at the mouth of Myrtos river and the shelter in Ferma (Ag. Ioannis small craft harbour) in a rocky outcrop coastal area. No boats were docked in either harbour, neither at the time of the earthquake nor the day the reconnaissance team visited the sites. In Myrtos, all local residents we spoke to were in the fields inland at the time of the earthquake, and none reported the sighting of the tsunami. At the small craft shelter of Ag. Ioannis, a distinct wrack line was identified 10 m away from the rocky shoreline, and 13 cm above the sea level at the time of the earthquake. The team could not identify any local resident observing the sea after the earthquake to confirm that the wrack line formed as a result of tsunami runup.

D7 Makry Gialos

Makry Gialos was the easternmost coastal location surveyed, about 21 km east of Ierapetra. The team interviewed one eyewitness who was in the fields at the time of the earthquake, but came back to her beachfront house approximately 20 min later and saw the shoreline advancing. She indicated the horizontal reach of the water level rise by pointing to a clear wrack line on the beach just north of the local harbour (Limanaki Beach); 0.35 m runup was measured here (Fig. A7e). The eyewitness described that the tsunami nearshore effects were noticeable at least until 18:00 local time and that she was told that the water level in the harbour dropped up to approximately 30 cm during the tsunami.

D8 Chrisi

The island of Chrisi lies 14 km (7.5 nautical miles) south of Ierapetra and is the nearest location to the earthquake epicentre. It is a popular tourist destination in the summertime due to its pristine beaches, with hundreds of tourists visiting daily via boats leaving from Ierapetra and unloading passengers in a small shelter on the south side of the island. While it has no permanent residents, there is a small group of people living there during winter time. At the time of the earthquake and the day of our visit, five people were living in a building on the north side of the island next to a small craft shelter.

The locals on the north side described the water level first rising 30–40 cm and then the beach shoreline withdrawing. The first withdrawal and the second rise were described as the largest observed. Only one eyewitness noted that he moved to higher ground during the water level

fluctuations. The eyewitnesses pointed to a precise runup location right at a step on the corner of a stone wall running across the perimeter of the dock (Figs A7f and A9b), which was confirmed also through a picture provided by the eyewitness showing that the gravel on the dock got wet up to that point. The eyewitnesses also pointed to the minimum drawdown point in the small harbour, which was measured with the GNSS system at −86 cm relative to the sea level at the time of the earthquake. The original pictures captured by the eyewitnesses with a cellphone during the tsunami were shared with us, and thus we were able to extract water level information with precise timestamps (see Appendix E).

A resident living in a makeshift house on the south side of the island indicated where the water level reached on Vlychada beach. The resident did-not feel the earthquake shaking and did not witness the tsunami, but was able to identify the tsunami runup wrack line the following day, after he was informed of the tsunami occurrence (Fig. A7g).

APPENDIX E: EYEWITNESS IMAGE ANALYSIS

The authors were able to get hold of two of the original videos that include the original timestamp. A series of original still images taken by an eyewitness, capturing the tsunami effects in a small craft shelter in north Chrisi were also shared with us. The original material includes valuable information on the timing and amplitude of the tsunami in these two coastal locations, that can benefit this study. It should be noted that the authors have not verified that the clock on the phones used to record the tsunami effects was correctly adjusted, however, smartphones typically have a self-adjusting clock. The water level was extracted through *in situ* topographic measurements using the GNSS system for the pictures in which the water level had reached the elevation of a recognizable topographic feature, whereas the water level was extracted through image analysis for all the other pictures/video frames.

The image analysis methodology followed previous studies analysing eyewitness still images and videos of past tsunamis (Fritz *et al.* 2006, 2012; Kalligeris *et al.* 2016). Extracting the sea level from the eyewitness images required a series of steps: (i) if possible, determine the camera intrinsic parameters (primarily lens distortion parameters), (ii) determine camera extrinsic parameters, that is, the position and orientation of the camera in space, through ground control points (GCP's) of known image and world coordinates and (iii) transform the image coordinates of water level points to world coordinates and extract the elevation value. The series of analysed pictures and the resulting water level readings for both the water levels extracted directly through *in situ* topographic measurements and through image analysis are shown in Fig. A8. More details on the image analysis methodology are provided in the following subsection.

E1 Image analysis methodology

For the analysis of the Chrisi images, we got hold of the same cellphone model to calibrate the camera in the lab and obtain the intrinsic parameters to remove the lens distortion using the toolbox of Bouguet (2008); for the two Arvi videos, the distorted image coordinates were used. We then applied the pinhole model, which relates image (p, q) to world (x, y, z) coordinates in the form of the direct linear transformation equations (Holland *et al.* 1997)

$$p = \frac{xL_1 + yL_2 + zL_3 + L_4}{xL_9 + yL_{10} + zL_{11} + 1}, \quad q = \frac{xL_5 + yL_6 + zL_7 + L_8}{xL_9 + yL_{10} + zL_{11} + 1}, \tag{E1}$$

where $L_j, j = 1,..., 11$ are the DLT coefficients. Rewriting eq. (E1) as a system of linear equations of the form $\mathbf{A} \cdot \vec{x} = \vec{b}$, allows to obtain the least square solution of DLT coefficients using at least 10 non-coplanar GCP's.

In order to have a large number of GCP's available for the extrinsic camera parametrization, we used the drone to build high-resolution point clouds and orthophotos for the harbours of Arvi and Chrisi. The drone flight tracks were programmed using the Pix4D software (Pix4D 2017). For the larger harbour of Arvi, we did two flight surveys: the first survey covered the entire harbour, and the second higher resolution flight survey covered the inner harbour captured in the eyewitness videos. The drone images captured at 5472 × 3748 resolution were post-processed using the Agisoft Photoscan software (Agisoft 2016) to produce high-resolution point clouds, and the data were geo-referenced using GCP's (in the form of targets on the ground) of known world coordinates. The flight parameters and the resolution of the resulting point clouds are given in Table A2. The ground control points used for the point cloud geo-referencing and the resulting orthophotos are shown in Fig. A9.

The GCP's for the camera extrinsic parametrization were extracted from the point clouds in each location, using elevations referenced to the sea level at the time of the earthquake. Backprojecting the GCP world coordinates to image coordinates using the best-fitting DLT coefficients provided the error statistics of the transformation. The error of the transformation reported here was estimated by displacing the point of interest by the mean pixel error of the backprojection and reading the range of resulting values in world coordinates.

Once the DLT coefficients were known, the transformation from image to world coordinates is underdetermined using a single camera (2 equations with three unknowns). To reduce the number of unknowns to two, sea level image points were extracted along vertical docks with known x–y line coordinates; the line equations were defined using the orthophotos built for each location (Fig. A9). Using the line equation notation $y = ax + b$, the image coordinates (p, q) of sea level points identified from the images along docks were transformed to world coordinates by rewriting eq. (E1) as:

$$\begin{bmatrix} x \\ z \end{bmatrix} = \begin{bmatrix} [L_1 - L_9 p + a(L_2 - L_{10} p)] & [L_3 - L_{11} p] \\ [L_5 - L_9 q + a(L_6 - L_{10} q)] & [L_7 - L_{11} q] \end{bmatrix}^{-1} \begin{bmatrix} A \\ B \end{bmatrix}, \tag{E2}$$

where $A = p - L_4 - b(L_2 - L_{10} p)$ and $B = q - L_8 - b(L_6 - L_{10} q)$. Coordinate z provided the water level for each sea level image point.

APPENDIX F: NUMERICAL GRIDS

The relief grids used with the numerical models for this application are shown in Fig. A10. The data for the coarsest grid (grid A) of 1/16 arc min (∼115 m) resolution covering the source and study areas were directly extracted from the European Marine Observation and Data Network (EMODNet) 2018 DTM. The intermediate resolution grid (grid B) is the EMODNet grid interpolated to a 0.03 arcmin (∼55 m) cell size to cover the area between the island of Chrisi and Ierapetra. The high-resolution grid (grid C) is a product of various topographic and bathymetric data sets. The bathymetry for grid C is primarily built on the 1960 nautical chart of the Hellenic Hydrographic Service (HHS), covering the harbour and bay of Ierapetra. HHS provided the authors with an updated bathymetric grid using data inside and around the harbour collected in the 1990s, which was incorporated in the bathymetry of grid C. The primary source for the topography is a DTM of 2 m cell size covering the city of Ierapetra, created using a stereopair of aerial pictures; this topography raster was used for tsunami inundation modelling in the Poseidon EU DG-ECHO project (Synolakis *et al.* 2011; Flouri *et al.* 2013). Topography gaps were filled using a DTM produced by the Hellenic Cadastre with 5 m cell size. An additional higher resolution grid (grid D, Fig. A10) was created using the same input data as grid C; grid D was only used to identify the resonant modes of the harbour of Ierapetra (Section 5.3).

Grid A-COUL, is grid A converted to UTM (Cartesian) coordinates to be used with COULWAVE. The domain of grid A-COUL was interpolated to a 30 m cell size, taking also into account the higher resolution HHS bathymetric and DTM topographic data. Therefore, grid A-COUL resolves the Ierapetra harbour breakwater and nearshore bathymetry. A summary for the grids is provided in Table A3.